

1

2 ~~**The S/Z Relationship of Rimed Snow Particles**~~3 **On the S/Z Relationship for Rimed Snow Particles in the W-band**

4

5 Shelby Fuller ¹, Sam Marlow ¹, Samuel Haimov ¹, Matthew Burkhart ¹, Kevin Shaffer ¹, Austin6 Morgan ¹, and Jefferson R. Snider ^{1,2}

7

8 ¹ Department of Atmospheric Science, University of Wyoming, Laramie, WY

9

10

11

12 ² Corresponding Author, jsnider@uwyo.edu

13

14

15 Abstract

16 ~~Values of liquid equivalent snowfall rate (S) at a ground site, and microwave reflectivity~~
17 ~~(Z) retrieved above the ground site using an airborne W-band radar, were acquired during~~
18 ~~overflights.~~ Values of liquid-equivalent snowfall rate (S) at a ground site and microwave
19 reflectivity (Z) retrieved using an airborne W-band radar were acquired during overflights.
20 Temperature at the ground site was between -6 and -15 °C. At flight level, within clouds
21 containing ice and supercooled liquid water, the temperature was approximately 7 °C colder.
22 Additionally, airborne measurements of snow particle imagery were acquired. The images
23 demonstrate that most of the snow particles were rimed. ~~The S/Z pairs are generally consistent~~
24 ~~with a published S/Z relationship. The latter was developed with airborne measurements of snow~~
25 ~~particle imagery, which were used to calculate S, and coincident airborne W-band radar~~
26 ~~measurements, for Z. Both the previous work and this contribution indicate that most S/Z~~
27 ~~relationships developed for W-band radars underestimate S in situations with rimed snow~~
28 ~~particles and with $Z < 1 \text{ mm}^6 \cdot \text{m}^{-3}$.~~ A relatively small set of S/Z pairs (4) are available from the
29 overflights. Important distinctions between these measurements and those of Pokharel and Vali
30 (2011), who also reported S/Z pairs for rimed snow particles, are 1) the fewer number of data
31 pairs, 2) the method used to acquire S, and 3) the altitude of the Z retrievals. It also shown that a
32 computationally-based S/Z relationship applied in W-band retrievals can underestimate S by
33 approximately a factor of two when snowfall is produced by riming.

34

35 **1 - Introduction**

36 Improvement of methods used to measure snowfall and rainfall are an ongoing focus of
37 meteorological research. The various methods are ground-based instruments that evaluate the
38 mass of precipitation that falls into or onto a collector (precipitation gauges) (Brock and
39 Richardson 2001), ground-based radars (Wilson and Brandes 1979), and airborne and space-
40 borne radars (Matrosov 2007; Kulie and Bennartz 2009; Geerts et al. 2010; Skofronick-Jackson
41 et al. 2017). An objective of these approaches, whether used to make observations independent
42 of other methods (e.g., Kulie and Bennartz 2009), or as a component of multiple observations
43 (e.g., Cocks et al. 2016), is estimation of precipitation rate and accumulation.

44 Many studies have investigated using radar for evaluating rainfall (for a review see
45 Wilson and Brandes 1979). There are two approaches. The first is research, both observational
46 and computational, that probes the relationship between rainfall rate (R) and radar-measured
47 values of backscattered microwave power. The latter is commonly reported as an equivalent
48 radar reflectivity factor (Z_e). The second is operational in the sense that precipitation gauges are
49 used to calibrate measurements acquired using weather surveillance radars. Complications
50 associated with converting Z_e to R, or converting a radar reflectivity factor¹ (Z) to R, can be
51 grouped in four categories: 1) Inaccuracy in quantification of Z, 2) variation of the R/Z
52 relationship stemming from precipitation processes (e.g., ~~evaporation,~~ coalescence, and break
53 up), 3) difference between the volume of a radar range gate versus the much smaller volume of
54 atmosphere sampled as precipitation falls to a gauge, and 4) vertical displacement between a
55 radar range gate and a calibrating gauge, especially at far ranges.

¹ Radars are calibrated to report Z_e (Smith 1984). Herein, radar reflectivities are reported as $Z = Z_e$ and as $\text{dBZ} = 10\log_{10}(Z_e)$.

56 For situations with snowfall, methods employing either gauge or radar are associated
57 with complications beyond that incurred in rainfall (Matrosov 2007; Martinaitis et al. 2015;
58 Cocks et al. 2016). Problems associated with gauge measurements are wind-induced snow
59 particle undercatch, gauge capping, delayed registration, and blowing snow aliasing as snowfall.
60 Moreover, in a situation with snow particles most abundant within a radar range gate, compared
61 to rain drops, and where a measurement of Z is used to infer R via a R/Z relationship, the
62 resultant precipitation rate will likely be inaccurate. This is because hydrometeor shape, density,
63 and dielectric properties are all variable for snow particles while relatively invariant for rain
64 drops. Additionally, a snow particle's terminal fall speed varies with size (as is the case for
65 drops) and with particle shape and particle density. Going forward, we refer to the latter two
66 properties as shape and density.

67 The goals of this paper are as follows: 1) to describe measurements of undercatch-
68 corrected liquid-equivalent snowfall rate (S , mm h^{-1}) and how these were paired with W-band
69 measurements of reflectivity (Z , $\text{mm}^6 \text{m}^{-3}$); 2) to contrast the measurement-based S/Z pairs
70 against calculated S/Z relationships commonly applied in retrievals of S based on reflectivity;
71 and 3) to investigate why the acquired data set deviates from predictions of some calculated S/Z
72 relationships.

73 In calculations of Z and liquid-equivalent snowfall rate, ~~(S), obtained for the operating~~
74 ~~wavelength of the nadir-looking radar carried on the CloudSat satellite (wavelength $\lambda = 3.2 \text{ mm}$),~~
75 density is an important parameter. In these calculations, density is commonly estimated using
76 empirical data (Matrosov 2007; Kulie and Bennartz 2009; Pokharel and Vali 2011, [PV11]). For
77 graupel, a snow particle that grows via collection of supercooled cloud droplets in a process
78 commonly referred to as riming, paired observations of particle mass and particle size have been

79 used to estimate density. There is considerable uncertainty in this approach. Based on data
80 collected at two northwestern US surface sites (Zikmunda and Vali 1972; Locatelli and Hobbs
81 1974), density values differ by at least a factor of two at particle sizes smaller than 2000 μm
82 (PV11; their Figure 4). Given that the density of rime ice varies with droplet impact speed,
83 droplet size, and temperature (Macklin 1962), it is not surprising that the density-versus-size
84 relationships analyzed by PV11 are so varied.

~~85 Our work analyzes values of Z acquired using an airborne radar that operates in the W-
86 band ($\lambda = 3.2$ mm). In satellite, airborne, and ground installations, W band radars are used to
87 retrieve Z and the latter is converted to S using a S/Z relationship. W band S/Z relationships are
88 developed in Matrosov (2007), Kulie and Bennartz (2009), Geerts et al. (2010), and PV11. This
89 contribution attempts to refine estimates of S based on W band radar observations and
90 particularly where the dominant particle type is either rimed crystals or graupel.~~

91 The following introductory paragraphs overview W-band S/Z relationships being applied
92 in instances of snowfall where mass is acquired by vapor deposition (crystal), by collection of
93 crystals (aggregate), and by riming (rimed crystal and graupel). Henceforth, the latter two snow
94 particle types are collectively referred to as rimed snow particles.

~~95 In a computational study, Matrosov (2007) reported an upper limit and a lower limit S/Z
96 relationship for both the crystal and aggregate particle types. Both were modeled as oblate
97 spheroids. The upper limit and a lower limit relationships are $S = 0.11 \cdot Z^{+2.5}$ and $S = 0.041 \cdot Z^{+2.5}$.
98 At any value of Z these differ by a factor of 2.7. This variance stems from changes in density,
99 shape, and fall speed as these changes are propagated through cloud microphysical and
100 microwave scattering computations. Similar analyses were conducted by Kulie and Bennartz~~

101 ~~(2009). Both Matrosov (2007) and Kulie and Bennartz (2009) state that the S/Z relationships~~
102 ~~they recommend should be applied cautiously in settings where rimed snow particles dominate.~~

103 In a computational study, Hiley et al. (2011) considered a variety of snow particle types
104 (column, plate, bullet rosette, sector plate, dendrite, and aggregate), employed a parameterized
105 ice particle size distribution (PSD) function (Field et al. 2005), accounted for a range of
106 temperature (-5 to -15 °C) via the Field et al. parameterization, and developed a range of S/Z
107 relationships for snow particles. Except for the aggregates, the modeled particle types were
108 crystals. Hiley et al.'s upper- and lower-limit relationships are $S = 0.21 \cdot Z^{0.77}$ and $S = 0.024 \cdot Z^{0.91}$.
109 Matrosov (2007) developed a range of S/Z relationships for aggregates. In that work, PSDs from
110 Braham (1990) were employed, and a range of particle aspect ratios and densities were factored
111 into the calculations. For aggregates, the S/Z relationship is $S = 0.056 \cdot Z^{1.25}$ and the upper- and
112 lower-limit S/Z relationships are $S = 0.11 \cdot Z^{1.25}$ and $S = 0.041 \cdot Z^{1.25}$ (Matrosov 2007). It should be
113 noted that Hiley et al. (2011) and Matrosov (2007) employed similar, but not identical,
114 computational methods and parameterized mass-size relationships. Kulie and Bennartz (2009)
115 developed an S/Z relationship for what they referred as a “snow particle” type. The wavelength-
116 dependent density derived by Surussavadee and Staelin (2007) (200 kg m^{-3} at $\lambda = 3.2 \text{ mm}$) was
117 adopted, the snow particles were modeled as spheres, and the Field et al. parameterization was
118 applied. The S/Z relationship developed for this particle type is $S = 0.52 \cdot Z^{0.83}$ (Surussavadee and
119 Staelin 2007; Kulie and Bennartz 2009; henceforth SSKB). Variance in the calculations
120 discussed in this paragraph originate from changes in density, shape, fall speed, and PSD as these
121 changes are propagated through the cloud-microphysical and microwave-scattering calculations.

122 In a hybrid approach (computational and an analysis of airborne observations), PV11
123 concluded that most of the snow particles they imaged were rimed snow particles. Their

124 calculations of S and Z, conducted using two density-size relationships (indicated with ρ_1 and
125 ρ_3), were also presented. They compared their calculated reflectivities to measurements of Z
126 from a W-band radar. That led to their conclusion that “...the lower density assumption...yielded
127 closer correspondence to observed reflectivities.” Their recommendation for S as a function of Z
128 - hereafter the $S(\rho_1)/Z$ best-fit line relationship - is $S = 0.39 \cdot Z^{0.58}$. In addition to variance in their
129 values of S, coming from a dependence on density, PV11 state that a value of S derived via their
130 ~~$S(\rho_1)/Z$ relationship best-fit line~~ is uncertain by a factor-of-ten. ~~This uncertainty is evident in the~~
131 ~~variance seen about the $S(\rho_1)/Z$ relationship in Fig. 11 of PV11. That uncertainty is evident in the~~
132 ~~variance seen about the line in Fig. 11 of PV11.~~ Those investigators, and Geerts et al. (2010),
133 attributed the variance to use of two-dimensional snow particle imagery in calculations of S and
134 to actual variations of density and shape not accounted for in the calculations. ~~Error associated~~
135 ~~with the radar retrieved reflectivities reported in PV11 contributed only marginally to the factor-~~
136 ~~of ten uncertainty.~~

137 ~~Our focus is the W band S/Z relationship for rimed snow particles. Section 2 describes~~
138 ~~the setting of our study, the instruments we deployed, and recordings we obtained using two data~~
139 ~~acquisition systems. One of the data systems was operated at a ground site and the other on an~~
140 ~~aircraft. Section 3 is an analysis of the recordings; this section also considers recordings from~~
141 ~~two additional, but ancillary, ground sites. Our findings are discussed in Sect. 4 and summarized~~
142 ~~in Sect. 5. An Appendix (Sect. 6) explains how we averaged recordings of near surface W band~~
143 ~~reflectivities and surface based recordings of snowfall.~~

144 Our focus is on surface measurements of S and on pairing of those measurements with
145 airborne measurements of Z. We also analyze airborne measurements of snow particle imagery.
146 The latter demonstrates that the particles observed at flight level were rimed. These

147 measurements are the basis for our assertion that our data set is relevant to ongoing
148 investigations of using Z to evaluate S in situations where precipitation is produced by riming.

149 Section 2 describes the setting of our study, the instruments we deployed, and recordings
150 we obtained using two data acquisition systems. One of the data systems was operated at a
151 ground site and the other on an aircraft. Section 3 is an analysis of the recordings; this section
152 also considers recordings from two additional, but ancillary, ground sites. Our findings are
153 discussed in Sect. 4 and summarized in Sect. 5. An Appendix (Sect. 6) explains how we
154 averaged recordings of near-surface W-band reflectivities and surface-based recordings of
155 snowfall.

156 2 - Site, Aircraft, and Instruments

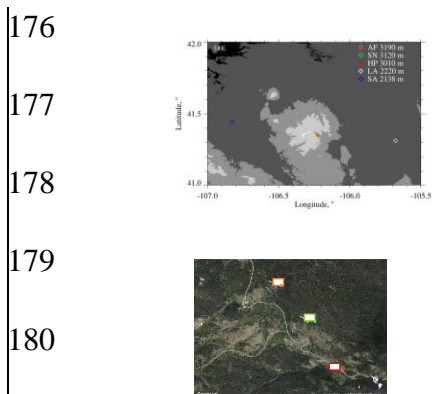
157 2.1 - Site

158 We analyzed aircraft and ground data from 14/15 December 2016, when the analyzed
159 snowfall event spanned a UTC date change, and from 3 January 2017. The ground data were
160 acquired in a forest/prairie ecotone on the eastern slope of the Medicine Bow Mountains in
161 southeastern Wyoming (Figs. 1a-b). No ground-based observers were deployed during the two
162 snowfall events we analyzed.

163 At one of three ground sites (HP in Figs. 1a-b) we deployed a hotplate precipitation
164 gauge (Rasmussen et al. 2011; Zelasko et al. 2018), a GPS receiver, and a data acquisition
165 system. Once per second, the data system ingested a hotplate-generated data string, combined
166 that with time-of-day from the GPS receiver (Coordinated Universal Time (UTC)), and recorded
167 the merged hotplate/UTC data string. The absolute accuracy of the ~~GPS~~-time stamp is no worse
168 than 2 s.

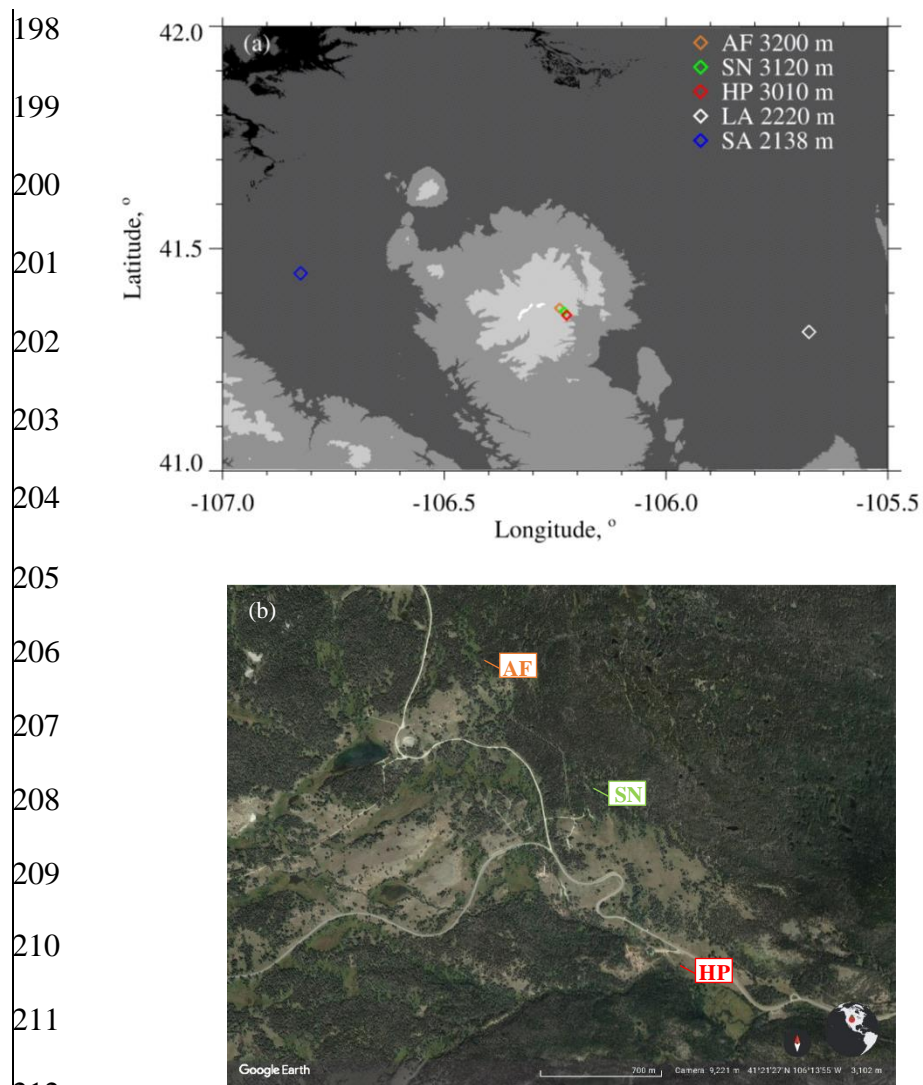
169 Overflights of the hotplate were done by the University of Wyoming King Air (WKA) on
170 14/15 December 2016 and on 3 January 2017. Data acquisition on the WKA was also
171 synchronized with UTC, but with much better accuracy than at the hotplate. Measurements of
172 wind (speed and direction), temperature, ~~and~~-relative humidity, ~~and~~ pressure from the US-GLE
173 AmeriFlux tower (AF in Figs. 1a-b) are also components of our analysis. The AmeriFlux data
174 were provided to us as 30-minute averages (AmeriFlux 2021; Marlow et al. 2023~~2~~).

175



THE REVISED FIGURE IS BELOW.

Figure 1—(a) Southeast Wyoming, airports near the communities of Saratoga, WY (SA) and Laramie, WY (LA), and the ground sites: AF = US GLE AmeriFlux tower, SN = Brooklyn Lake SNOTEL, and HP = hotplate. Altitudes of the airports and ground sites are in the legend. Altitude thresholds for the digital elevation map are 1500, 2000, 2500, 3000, and 3500 meters. (b) Close up of the AF, SN, and HP ground sites (from © Google Earth).



213 Figure 1 – (a) Southeast Wyoming, airport at Saratoga, WY (SA), airport at Laramie, WY (LA),
 214 and the ground sites: AF = US-GLE AmeriFlux tower, SN = Brooklyn Lake SNOTEL, and HP =
 215 hotplate. Altitudes of the airports and ground sites are in the legend. Altitude thresholds for the
 216 digital elevation map are 1500, 2000, 2500, 3000, and 3500 meters. (b) Close up of the AF, SN,
 217 and HP ground sites (from © Google Earth).

218

219
220 **2.2 - University of Wyoming King Air (WKA)**

221 We analyzed the following WKA measurements: aircraft position, ~~ambient~~ temperature,
222 snow particle imagery, and three moments of the cloud droplet size distribution. A
223 Cloud Droplet Probe (CDP; Faber et al. 2018) was the basis for the droplet size distribution
224 measurements and the derived moments. The latter are droplet concentration (N), cloud liquid
225 water content (LWC), and mean droplet diameter ($\langle D \rangle$). Snow particle imagery was obtained
226 using a precipitation particle imaging probe (2DP; Korolev et al. 2011) and a cloud particle
227 imaging probe (2DS; Lawson et al. 2006). These acquired two-dimensional images of particles
228 between 200 to 6400 μm (2DP) and between 10 to 1280 μm (2DS).

229 **2.3 - The W-band Wyoming Cloud Radar (WCR)**

230 ~~Measurements from the Wyoming Cloud Radar (WCR), operated on the WKA, were also~~
231 ~~analyzed. We analyzed values of the vertical component snow particle Doppler velocity~~
232 ~~retrieved from below the WKA using the WCR's down-looking antenna. Our starting point for~~
233 ~~that analysis is the Level 2 WCR data which has snow particle Doppler velocities corrected for~~
234 ~~aircraft motion (Haimov and Rodi 2013). Retrievals from the up-looking and down-looking~~
235 ~~antennas of the WCR, operated on the WKA, were also analyzed. For this we used Level 2 WCR~~
236 ~~data² with reflectivities recorded as $dBZ = 10 \cdot \log_{10}(Z)$. The reflectivities were converted from~~
237 ~~dBZ to Z prior to processing. Additionally, values of the vertical-component Doppler velocity~~
238 ~~retrieved from below the WKA using the WCR's down-looking antenna were analyzed. The~~
239 ~~Doppler velocities were corrected for aircraft motion, as described in Haimov and Rodi (2013).~~
240 We use V_D to symbolize the corrected vertical-component Doppler velocity and adopt the

² http://flights.uwyo.edu/uwka/wcr/projects/snowie17/PROCESSED_DATA/

241 convention that $V_D > 0$ indicates upward hydrometeor snow-particle motion. Level 2 values of Z
242 ~~retrieved using the up-looking and down-looking WCR antennas were also analyzed.~~

243 The Level 2 WCR sampling was different on the two flight days and this difference is
244 indicated in Table 1. The flights were conducted in preparation for the SNOWIE field project
245 (Tessendorf et al. 2019) and were flown from the Laramie, WY Airport (“LA” in Fig. 1a).

246 Ground-based calibrations of the WCR’s up-looking antenna and correlations between in-
247 flight retrievals acquired using the WCR’s up-looking and down-looking antennas were used to
248 estimate the absolute accuracy of the WCR-derived values of dBZ. This is ± 2.5 dBZ (PV11).

249

250

251 Table 1 – Level 2 WCR sampling and the WKA overflight time

Date	Level 2 WCR Vertical Sampling, m	Level 2 WCR Along-track Sampling, s	Overflight Time, UTC
14/15 December 2016	23	0.23	00:00:38 (15 December 2016)
3 January 2017	30	0.36	20:32:03

252

253

254 2.4 - Hotplate Gauge

255 Algorithms used to process hotplate measurements are described in Rasmussen et al.
256 (2011), Boudala et al. (2014), and Zelasko et al. (2018). Henceforth, these are referred to as R11,
257 B14, and Z18, respectively. ~~In this section, we describe how we analyzed hotplate measurements~~
258 ~~acquired at the HP site.~~ This section describes how hotplate measurements acquired at the HP site
259 were analyzed.

260 Four measurements fundamental to the steady state energy budget of the hotplate's
261 temperature-controlled up-viewing plate are output by the hotplate microprocessor as one-minute
262 running averages (Z18). These ~~running~~ averages were merged with the GPS time and recorded at
263 1 Hz by the data acquisition system (Sect. 2.1). The four measurements are electrical power
264 supplied to the plate, ambient temperature, wind speed, and solar irradiance. With these
265 measurements, calibration data (Marlow et al. 2023~~2~~), and the algorithm described in Z18, we
266 calculated the liquid-equivalent snowfall rate. The latter is not corrected for the snow particle
267 undercatch-; however, in what follows we describe that correction.

268 Marlow et al. (2023~~2~~; their Figure 4b) report the relationship between snow particle catch
269 efficiency and wind speed that we applied in calculations of the undercatch-corrected liquid-
270 equivalent snowfall rate (~~S , mm h^{-1}~~). There are three bases for this relationship. ~~The first~~ is the
271 catch efficiencies R11 derived from measurements they obtained using a weighing gauge
272 operated within a double fence intercomparison reference shield and ~~a hotplate gauge collocated~~
273 ~~measurements from an unshielded hotplate gauge.~~ R11 ~~plotted their hotplate catch efficiencies~~
274 ~~versus wind speeds measured at 10 m AGL (their Figure 8).~~ We symbolize these paired
275 measurements as SRG (shielded reference gauge) and UHG (unshielded hotplate gauge). R11
276 plotted hotplate catch efficiencies (i.e., UHG/SRG) versus wind speeds measured at 10 m AGL

277 (their Fig. 8). ~~S~~The second is Marlow et al.'s adjustment of R11's 10 m AGL wind speeds to 2 m
278 AGL. The basis for that adjustment is surface boundary layer parameters derived for R11's site
279 (Kochendorfer et al. 2018) ~~and Panofsky and Dutton (1984; their Eq. 6.7)~~ and an equation from
280 Panofsky and Dutton (1984; their Eq. 6.7). The adjustment was made because the hotplate-
281 reported wind speeds, both here and in Marlow et al. (2023~~2~~), were acquired at approximately 2
282 m above the snowpack surface. ~~The third is a validation of the Marlow et al. (2022) undercatch~~
283 ~~relationship. That was done by comparing values of S from the hotplate gauge and a SNOTEL~~
284 ~~pillow gauge (Serreze et al. 1999). In that validation (Marlow et al. 2022; their Figure 10a), the~~
285 ~~SNOTEL pillow gauge was at the SN site and the hotplate was at the HP site. The SN and HP~~
286 ~~sites are in Figs. 1a-b.~~ Third is Marlow et al.'s comparison of SNOTEL-derived snow water
287 equivalent depth changes and hotplate-derived time-integrated accumulations. The time base for
288 the comparisons was 24 hours. Based on that comparison, which has 57 paired values acquired at
289 the sites labeled HP and SN in Fig. 1, the average fractional absolute relative difference is 0.30.
290 In the Marlow et al. (2023) comparison (their Fig. 9a), at accumulation = 10 mm, imprecision
291 associated with the SNOTEL measurement corresponds to a relative error which is 0.24 (Marlow
292 et al. 2023). This indicates that SNOTEL contributed significantly to the previously-mentioned
293 relative difference and especially so for the smaller accumulations in Figure 9a of Marlow et al.
294 (2023). Because of this, we did not limit calculation of the relative difference to a subset of the
295 57 paired measurements. Based on this assessment of the relative difference, the hotplate
296 precision applied in this analysis was taken to be 0.3.

297 ~~We also analyzed values of wind speed output by the hotplate microprocessor (U_{PRO}).~~
298 The hotplate-derived wind speeds acquired at ~ 2 m, and discussed in the previous paragraph, are
299 henceforth symbolized U_{PRO} . The basis for these ~~is hotplate derived wind speed~~ is a steady state

300 energy budget of the hotplate's temperature-controlled down-viewing plate and a proprietary
301 algorithm (R11 and Z18). The U_{PRO} were reported by the hotplate as one-minute running
302 averages (Z18) and we recorded these at 1 Hz. Examples are the gray dots in Fig. 2.
303 Additionally, we calculated and analyzed one-minute-averaged values of U_{PRO} and the
304 corresponding standard deviations. Examples of these are the black circles and the short vertical
305 line segments, ~~respectively,~~ in Fig. 2.

306

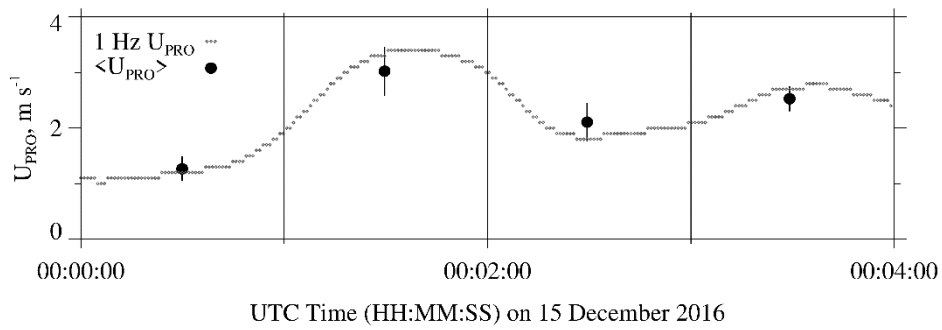
307

308

309

310

311



312 Figure 2 – Hotplate wind speed measurements (U_{PRO}) 00:00:00 to 00:04:00 on 15 December

313 2016. Gray dots are the one-minute running-average U_{PRO} recorded at 1 Hz. Black circles are the

314 one-minute-averaged U_{PRO} (± 1 standard deviation).

315

316 3 - Analysis

317 3.1 - WKA Overflight Time

318 The focus of our analysis is the two WKA flight segments shown in Figs. 3a-b. The maps
319 shown in the figures have the three ground sites (AF, SN, and HP) and the WKA flight tracks
320 (white line). The beginning-to-end time interval for the flight tracks is 100 s and these are
321 divided into ten 10-second intervals. The 10 s intervals are indicated with white diamonds. ~~With~~
322 ~~the exception of~~ Except for the turn evident in Fig. 3b, the flight tracks are straight ~~and level~~,
323 and the track direction is approximately upwind to downwind.

324 Times that the WKA was closest to the HP site were evaluated by finding the point on the
325 flight track where the horizontal position of the WKA was closest to the hotplate's coordinates.
326 These times are symbolized t_o and are referred to as overflight times. In Figs. 3a-b the
327 downwind end of the flight tracks end at the overflight time. The latitude/longitude position of
328 the aircraft was within 390 m of the hotplate at the overflight times. Table 1 has the overflight
329 times on the two flight days.

330

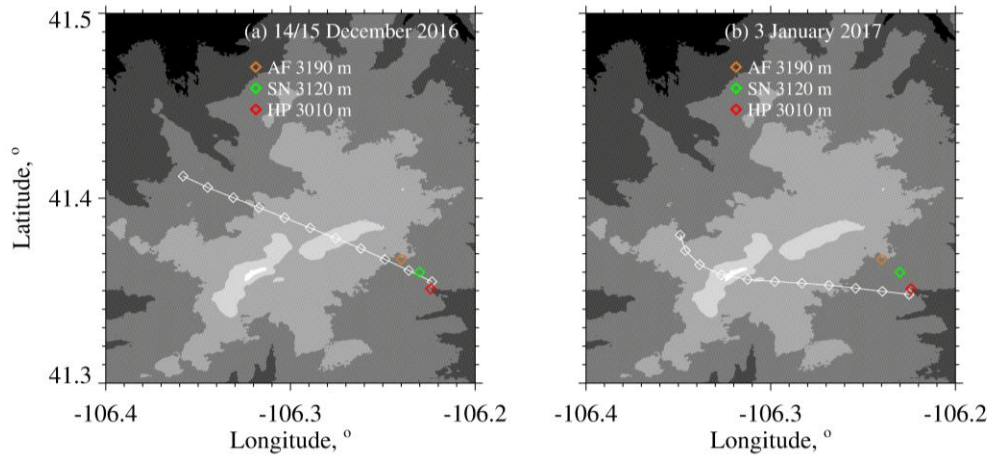


Figure 3 – (a) WKA flight track on 14/15 December 2016 for time interval = overflight time - 100 s to the overflight time. (b) WKA flight track on 3 January 2017 for time interval = overflight time - 100 s to the overflight time. The white diamonds on the tracks are separated, in time, by 10 s. Altitude thresholds for the digital elevation maps are 2600, 2800, 3000, 3200, 3400, and 3600 meters. Altitudes of the ground sites are in the legend.

3.2 – Effect of Attenuation on WCR Reflectivities

(NOTE: Table 3 is at the end of the manuscript)

The presence of water vapor, cloud water, and snow particles within the WCR's transmission path will contribute to an attenuation of microwave intensity and will therefore negatively bias the retrieved reflectivities (Matrosov 2007; Hiley et al. 2011; Kneifel et al. 2015). We used *in situ* measurements, and models of attenuation, to estimate this bias. For vapor, we used temperature (T), relative humidity (RH), and pressure (P) measurements from the AF (Table 2) and an equation for the extinction coefficient (Ulaby et al. 1981; their Eq. 5.22). For cloud water, we used T and LWC measurements from the WKA and a parameterized extinction coefficient (Liebe et al. 1989; Vali and Haimov 2001). For snow particles, we used 2DP-derived snow particle mass concentrations, from the WKA, and extinction measurements from Nemarich et. al (1988). The snow mass concentrations were evaluated as the product of the 2DP-derived snow particle volume - assuming spheres - and a snow particle density $\rho = 210 \text{ kg m}^{-3}$. This estimate of density comes from PV11's ρ_1 formula evaluated at $D = 1 \text{ mm}$. Vapor, cloud water, and ice particle concentrations applied in the calculations are in the second to fourth columns of Table 3. These are the maxima of measurements acquired between $t_o - 10 \text{ s}$ and t_o . This time interval is nearly the same as the combined durations of the two WCR averaging intervals analyzed in Sect. 3.5. The fifth to seventh columns have the one-way transmission pathlengths. For cloud water, this is the vertical distance between cloud base [derived thermodynamically using AF measurements (Table 2)] and the flight level, and for both vapor and snow particles this is the vertical distance between the hotplate and the flight level. (Aircraft and HP altitudes

368 are in Table 2 and Fig. 3.) It was assumed that the measured mass concentrations (vapor, cloud
369 water, and snow particles) were uniform over the prescribed pathlengths. Finally, our use of
370 vapor density from the AF ground site is estimated to have caused the vapor-induced
371 attenuations to be overestimated by approximately 50 %. Two-way attenuations ($\Delta(dB)$),
372 summed over contributions from the three components, are presented in the final column.
373 Fortuitously, these are equal on the two days but with vapor and snow particles dominating on
374 December 15 and with liquid water dominating on January 3. Attenuation-corrected reflectivities
375 (Z') were derived using the uncorrected reflectivities (Z) and the $\Delta(dB)$

$$376 \quad Z' = 10^{\left[\frac{10 \cdot \log_{10}(Z) + \Delta(dB)}{10}\right]} . \quad (1)$$

377

378 Table 2 – Atmospheric state averages

379

Date	WKA ^a Track Altitude, m	WKA ^a T, °C	AF ^b T, °C	AF ^b RH, %	WKA ^{a,c} Track Vector	WKA ^{a,c} Wind Vector	AF ^{b,c} Wind Vector
14/15 December 2016	4546	-13.9	-6.3	86	310 / 130	274 / 32	250 / 8.5
3 January 2017	4196	-21.7	-14.6	77	280 / 120	265 / 27	260 / 5.4

380

381

382 ^a Altitude, temperature, track vector, and horizontal wind vector data obtained by averaging 1 Hz
383 WKA measurements. The averaging interval is 60 s and the interval starts at the overflight time,
384 minus 60 s, and ends at the overflight time.

385

386 ^b Temperature (T), relative humidity (RH), and horizontal wind vector data from sensors on the
387 US-GLE AmeriFlux tower (Sect. 2.1). The wind sensor was deployed at 26 m AGL (3223 m
388 MSL) and the T/RH sensor was deployed at 23 m AGL (3220 m MSL). The AF measurements
389 correspond to 30-minute averages closest to the overpass time. In the AF data set time stamps on
390 the relevant AF recordings are 00:00 UTC (15 December 2016) and 20:30 UTC (3 January
391 2017).

392

393 ^c Vectors are presented in the following format: Direction of motion (degree relative to true
394 north) / speed (m s^{-1}).

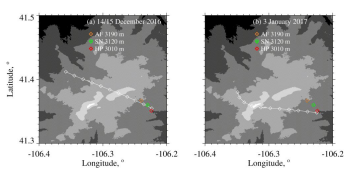
395

396

397 **3.32 - Correction of Doppler Velocity**

398 We accounted for bias in V_D (Sect. 2.3) due to deviation of the down-looking WCR
399 antenna from vertical. This was done by applying the correction described in Zaremba et al.
400 (2022) (their Eq. A4). The west-to-east and south-to-north particle velocities used in the
401 correction were assumed to be equal to component wind velocities. The latter were expressed as
402 linear functions of altitude using the information in the penultimate and last columns of Table 2.
403 The component velocities as functions of altitude and the linear equations relating velocity and
404 altitude are provided in the Appendix.

405



THE REVISED FIGURE IS ABOVE.

~~Figure 3—(a) WKA flight track on 14/15 December 2016 for time interval = overflight time—
100 s to the overflight time. (b) WKA flight track on 3 January 2017 for time interval =
overflight time—100 s to the overflight time. The white diamonds on the tracks are separated, in
time, by 10 s. Altitude thresholds for the digital elevation maps are 2600, 2800, 3000, 3200,
3400, and 3600 meters. Altitudes of the ground sites are in the legend.~~

420 Table 2—Aircraft and atmospheric state averages
421

Date	WKA ^a Track Altitude, m	WKA ^a T, °C	AF ^b T, °C	AF ^b RH, %	WKA ^{a,c} Track Vector	WKA ^{a,c} Wind Vector	AF ^{b,c} Wind Vector
14/15 December 2016	4546	-13.9	-6.3	86	310/130	274/32	250/8.5
3 January 2017	4196	-21.7	-14.6	77	280/120	265/27	260/5.4

422

423

424 ^a-Altitude, temperature, track vector, and horizontal wind vector data obtained by averaging 1-Hz WKA
425 measurements. The averaging interval is 60 s and the interval starts at the overflight time, minus 60 s, and
426 ends at the overflight time.

427

428 ^b-Temperature, relative humidity, and horizontal wind vector data from sensors on the US GLE
429 AmeriFlux tower (Sect. 2.1). The wind sensor was deployed at 26 m AGL (3223 m MSL) and the T/RH
430 sensor was deployed at 23 m AGL (3220 m MSL). The AF measurements correspond to 30-minute
431 averages closest to the overpass time. In the AF data set time stamps on the relevant AF recordings are
432 00:00 UTC (15 December 2016) and 20:30 UTC (3 January 2017).

433

434 ^c-Vectors are presented in the following format: Direction of motion (degree relative to true north) / speed
435 ($\text{m}\cdot\text{s}^{-1}$).

436

437
438
439
440
441
442
443

3.43 - Hotplate Measurement of Wind Speed

Here we compare the hotplate-derived wind speed ~~—symbolized U_{PRO} (Z18)—~~ to wind speed derived using an R.M.Young rotating anemometer (R.M.Young 2001). ~~The second of these two speeds we symbolize U_{RMY} and we note that the basis for the first (U_{PRO}) is a proprietary algorithm (Sect. 2.4).~~ The second of these is symbolized U_{RMY} and the basis for the first (U_{PRO}) is a proprietary algorithm (Sect. 2.4). We are doing this comparison because B14 showed that U_{PRO} can be high-biased, relative to a conventional anemometer, and because U_{PRO} is the primary determinant of the rate that the up-viewing plate dissipates sensible heat energy. Diagnosis of that heat transfer rate is our basis for calculating the liquid-equivalent snowfall rate (Z18). The U_{PRO} also determines the snow particle catch efficiency. The latter is our basis for calculating the undercatch-corrected liquid-equivalent snowfall rate (Sect. 2.4).

449
450
451
452
453
454
455
456
457
458

Three years before the wind speed comparison presented here, we attempted to compare the U_{PRO} reported by our hotplate³ and wind speed reported by a WXT520 Vaisala weather transmitter equipped with an ultrasonic anemometer (Vaisala 2012). These instruments were operated at the HP site in Fig. 1b. However, that data set was difficult to interpret because we did not correctly record the desired 1 Hz wind speed measurements from the WXT520. The comparison reported here was done at the Laramie, WY Airport in December 2019 and January 2020. Compared to the HP site, the Laramie Airport site (indicated LA in Fig. 1) is free of obstruction, out to 120 m, and experiences larger wind speeds. By mounting the hotplate and the R.M.Young anemometer on rigid metal pipes, the hotplate's heated horizontal surfaces (the up- and down-viewing plates seen in Figure 1 of Z18) and the anemometer's spinning axis (oriented

³ The hotplate used here is the device described in Wolfe and Snider (2012), in Z18, and in Marlow et al. (2023²).

459 horizontally) were both positioned at 2 m AGL. The pipes were separated horizontally by 5 m.
460 There was no precipitation on the days selected for the wind speed comparisons. The values of
461 U_{PRO} and U_{RMY} we analyzed were recorded with a data system that time stamped the 1 Hz U_{PRO}
462 and 1 Hz U_{RMY} with a relative timing accuracy no worse than 1 s.

463 A wind speed comparison - from 13 December 2019 - is shown in Fig. 4a. U_{PRO} was
464 brought into the comparison by sampling it once per minute from files containing 1 Hz
465 recordings of the one-minute running-average U_{PRO} (Sect. 2.4). U_{RMY} was brought into the
466 comparison by starting with files containing 1 Hz recordings and converting these to one-minute
467 averages. Fig. 4a shows no evidence of bias and Fig. 4b demonstrates that the average absolute
468 departure between the U_{PRO} and U_{RMY} (both one-minute averages) is no larger than 0.5 m s^{-1} .

469 Table 43 has eight more precipitation-free comparisons. Included in the table are temperature
470 and wind speed averaged over the comparison intervals (4 to 20 UTC), the slope of the linear-
471 least-squares fit line (forced through the origin, red line), and the lower and upper quartiles of the
472 slope. We calculated the quartiles using the method of Wolfe and Snider (2012). In contrast to
473 Figs. 4a-b, Figs. 4c-d make the comparison using 1 Hz values of U_{PRO} and U_{RMY} . The larger
474 scatter and larger average absolute departure seen in these panels is a consequence of the
475 hotplate's limited time response, compared to the R.M. Young. We quantify the hotplate's
476 response time in terms of a thermal response time. During wintertime at the Laramie Airport, and
477 with wind speed at 5 m s^{-1} , the down-viewing plate's thermal response time is 60 s (results not
478 shown). Because the temperature of down-viewing plate is actively controlled, this does not
479 translate to a 60 s lag between changes in wind speed and the hotplate response. The $U_{\text{PRO}}/U_{\text{RMY}}$
480 departure is most evident at $U_{\text{PRO}} > 5 \text{ m s}^{-1}$ (Fig. 4d) but this is not a concern for U_{PRO} on 14/15
481 December 2016 or on 3 January 2017. ~~As we show below, the U_{PRO} was less than 5 m s^{-1} at the~~

482 ~~hotplate during the two WKA overflights.~~ Snider (2023) demonstrated that the U_{PRO} was less
483 than 5 m s^{-1} at the hotplate during the two WKA overflights.

484

485

486

487

488

489

490

491

492

493

494

495

496

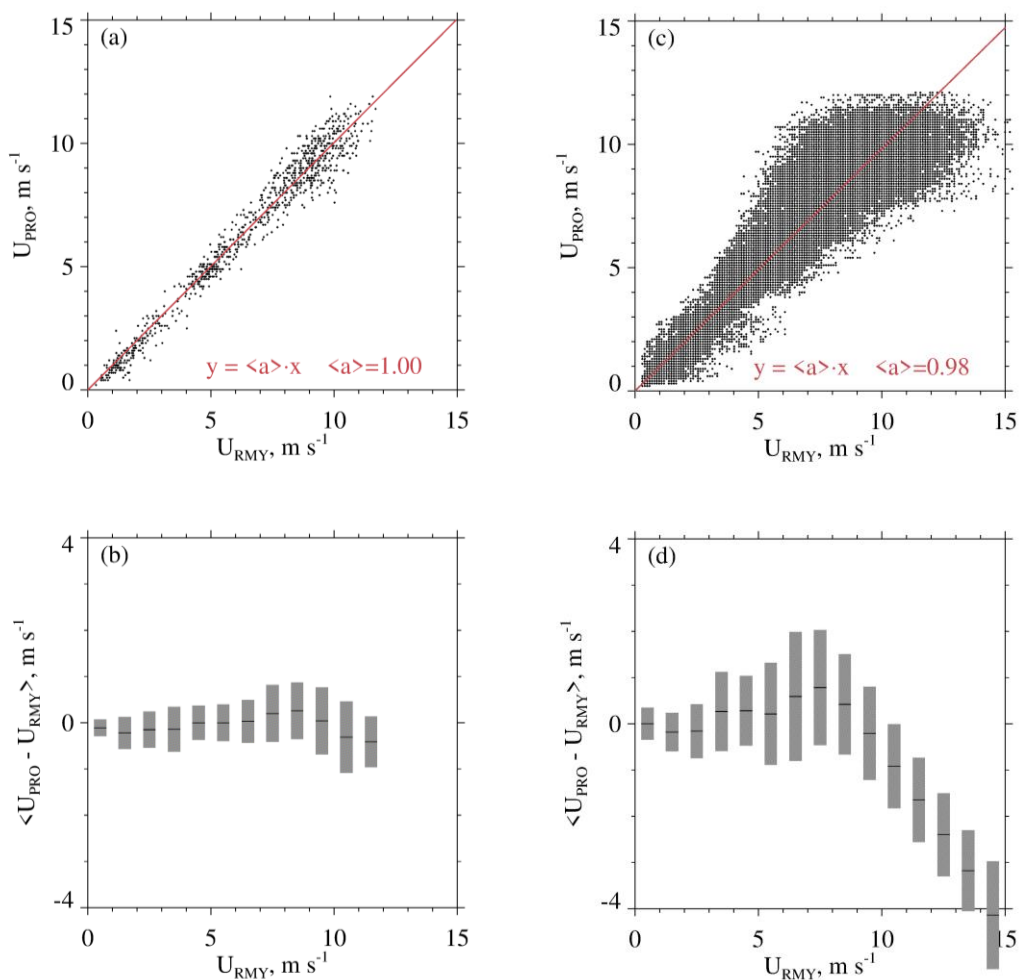
497

498

499

500

501



502 Figure 4 – (a) Scatterplot of one-minute-averaged U_{PRO} and one-minute-averaged U_{RMY} .

503 Measurements were acquired at the Laramie, WY Airport 13 December 2019. The red line is a

504 linear-least-squares fit line (forced through the origin). (b) Average departure between one-

505 minute-averaged U_{PRO} and one-minute-averaged U_{RMY} . Average departures are computed for

506 discrete U_{RMY} intervals and the averages are indicated with short black horizontal lines. Gray

507 bars indicate ± 1 standard deviation. (c) Same as in (a) except 1 Hz values of U_{PRO} and U_{RMY} . (d)

508 Same as in (b) except for 1 Hz values of U_{PRO} and U_{RMY} .

509

510

511 Table 43 - U_{PRO} versus U_{RMY} correlations

Date, UTC ¹	$\langle T \rangle^2$, °C	$\langle U \rangle^2$, m s ⁻¹	$\langle a \rangle^3$	a ⁴ First Quartile	a ⁴ Third Quartile
7 December 2019	-0.40	5.40	1.00	0.90	1.04
8 December 2019	2.70	4.10	0.99	0.90	1.04
10 December 2019	-5.20	3.80	0.99	0.83	1.04
13 December 2019	-1.50	6.60	1.00	0.93	1.06
18 December 2019	-6.20	3.60	0.99	0.92	1.04
19 December 2019	-6.90	2.70	0.95	0.84	0.99
6 January 2020	-6.40	8.80	1.01	0.96	1.06
8 January 2020	0.30	4.20	1.00	0.87	1.05
11 January 2020	-7.20	7.00	1.02	0.97	1.08

512

513

514 ¹ Statistics presented are based on one-minute-averaged U_{PRO} and one-minute-averaged U_{RMY}
515 measurements made between 04:00 to 20:00 UTC.

516

517 ² ~~Interval-averaged temperature~~ ~~Averaged temperature~~ and interval-averaged wind speed

518

519 ³ Slope of the one-minute-averaged U_{PRO} versus one-minute-averaged U_{RMY} linear-least-squares fit line,
520 forced through the origin

521

522 ⁴ Quartiles of the slope (see text)

523

524

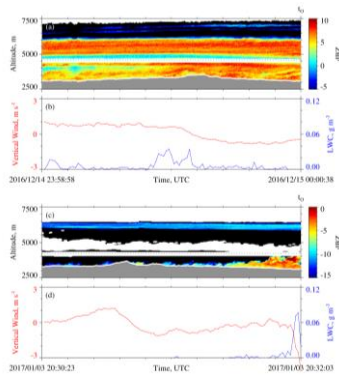
525
526
527
528
529
530
531
532
533
534
535
536
537
538
539
540
541
542
543
544
545
546
547

3.54 - Combined Aircraft and Surface Measurements ~~WCR Measurements~~

Figure 5 has WCR and WKA measurements starting 100 s prior to t_o and ~~ending~~ ~~completing~~ at t_o . The sequences in Figs. 5a and 5c are reflectivities from both the up- and down-looking antennas. In Fig. 5a the flight track (black dashed horizontal line) is at 4550 m and in Fig. 5c the flight track is at 4200 m. At the t_o in Fig. 5a, below the WKA, the maximum radar echo is +6 dBZ ($Z = 4 \text{ mm}^6 \text{ m}^{-3}$) while in Fig. 5c that maximum is -3 dBZ ($Z = 0.5 \text{ mm}^6 \text{ m}^{-3}$). Supercooled liquid water was detected as the aircraft approached the ridgeline (Fig. 5b) and during the last 3 seconds of the time sequence in Fig. 5d. During these encounters with supercooled liquid, the maximum LWC values were 0.03×10^{-3} and $0.08 \times 10^{-3} \text{ kg m}^{-3}$ on 14 December 2016 and 3 January 2017, respectively. Values of N (Sect. 2.2) at times of maximal LWC were 3×10^6 and $100 \times 10^6 \text{ m}^{-3}$ on 14 December 2016 and 3 January 2017, respectively. Even on 3 January 2017, the $\langle D \rangle$ (Sect. 2.2) associated with maximum LWC was sufficient for hexagonal plate crystals with diameter larger than $100 \text{ }\mu\text{m}$ to collide with the observed droplets with efficiencies > 0.1 (Wang and Ji 2000).

We temporally and spatially averaged the values of Z we compared with time-averaged values of S. There are two reasons for this: 1) As discussed in Sect. 3.1, the WCR did not sample Z exactly over the hotplate, and furthermore, the width of radar beam at 1500 m range - roughly the distance between the aircraft and the ground at the overflight times - is 30 m and thus considerably smaller than the minimum horizontal distance between the aircraft and the HP. 2) Compared to the WCR, the hotplate is a relatively slow-response measurement system whose output is commonly averaged over one-minute intervals (Z18).

548
 549
 550
 551
 552
 553
 554
 555
 556
 557
 558
 559
 560
 561
 562
 563
 564
 565
 566
 567
 568
 569
 570
 571
 572
 573
 574
 575



THE REVISED FIGURE IS BELOW.

Figure 5—(a) 100 s of WCR reflectivity from 14/15 December 2016 ending at t_0 . (b) 100 s of LWC and gust probe vertical wind velocity from 14/15 December 2016 ending at t_0 . (c) 100 s of WCR reflectivity from 3 January 2017 ending at t_0 . (d) 100 s of LWC and gust probe vertical wind velocity from 3 January 2017 ending at t_0 . In (a) and (c), above and below the flight track is the roughly 200-m-deep WCR blind zone, reflectivity above (below) the flight track is from the up-looking (down-looking) WCR antenna, black indicates reflectivity [dBZ] smaller than minimum indicated in the color bar, white immediately above the terrain indicates echo that was discarded because of ground clutter, and white above the ground clutter and outside of the blind zone indicate $\text{dBZ} < \text{minimum detectable signal}$.

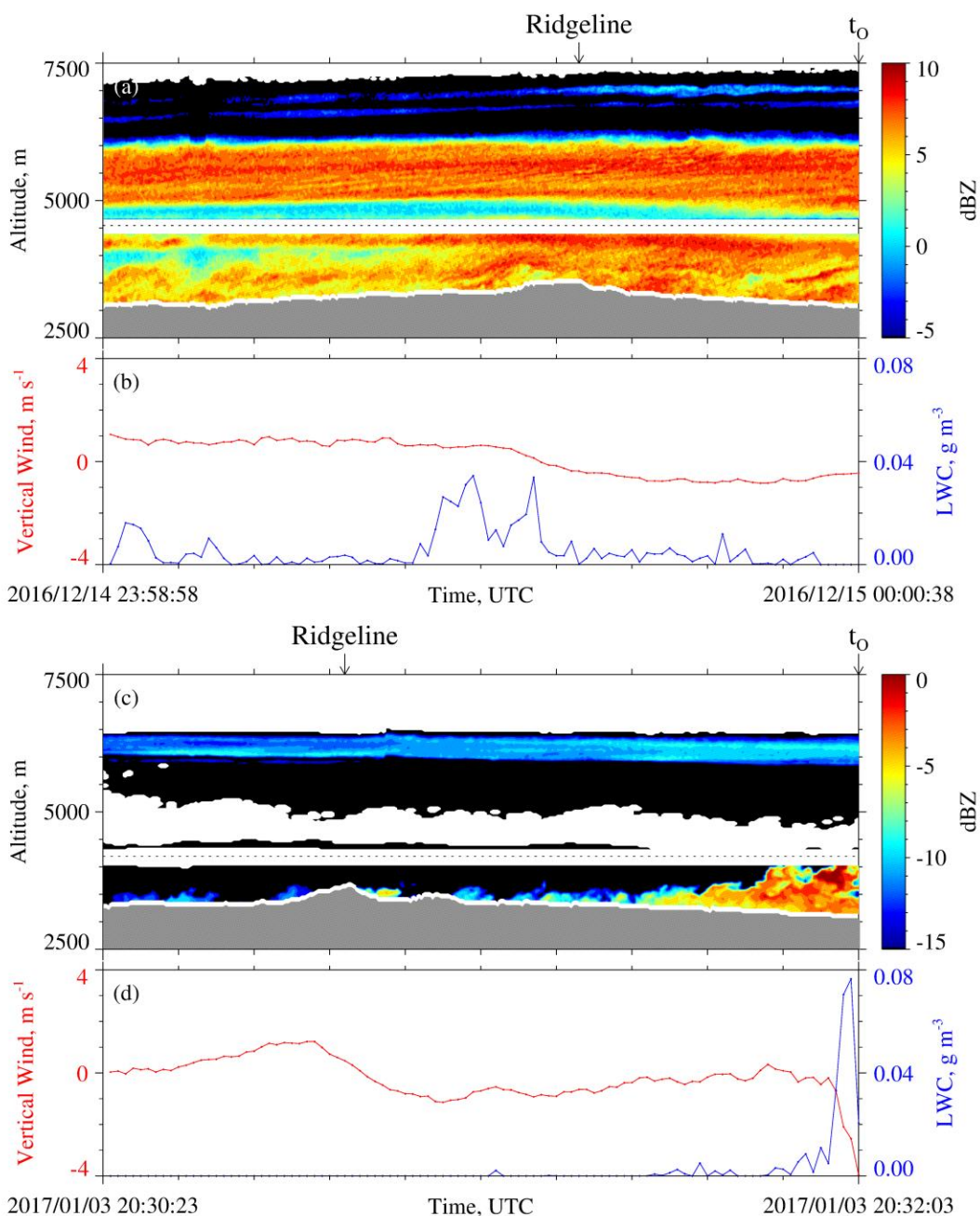


Figure 5 – (a) 100 s of WCR reflectivity and (b) 100 s of LWC and gust probe vertical wind velocity ending at t_o on 14/15 December 2016. (c) 100 s of WCR reflectivity and (d) 100 s of LWC and gust probe vertical wind velocity ending at t_o on 3 January 2017. In (a) and (c) above and below the flight track is the roughly 200-m-deep WCR blind zone, reflectivity above (below) the flight track is from the up-looking (down-looking) WCR antenna, black indicates dBZ values smaller than minimum indicated in the color bar, white immediately above the terrain indicates echo that was discarded because of ground clutter, and white above the ground clutter and outside of the blind zone indicate dBZ < minimum detectable signal.

621
 622 ~~Our averaging scheme starts with the HP averaging intervals begun at t_0 and at $t_0 + 60$~~
 623 ~~s. The duration of these intervals is one minute. Figure 6a is a schematic of an HP averaging~~
 624 ~~interval started at t_0 , Fig. 6b is a schematic of the corresponding WCR averaging domain, and~~
 625 ~~Figs. 6c-d are schematics of an adjacent averaging interval/domain. Figures 6a and 6c also show~~
 626 ~~that the indexes $i=0$ and $i=1$ are used to indicate HP averaging intervals begun at t_0 and $t_0 +$~~
 627 ~~60 s, respectively. Figures 7b and 8b show hotplate snowfall measurements from 14/15~~
 628 ~~December 2016 and 3 January 2017 and how we label the HP averaging intervals begun at t_0 .~~
 629 ~~In these and subsequent figures, colored circles surround the indexes, blue is used to color code~~
 630 ~~15 December 2016, and red is used to color code 3 January 2017. The Appendix explains the~~
 631 ~~averaging in greater detail. Two aspects not discussed here, but are discussed in the Appendix,~~
 632 ~~are how the “i” indexes were used to calculate the WCR averaging start and end times and how~~
 633 ~~the lines defining the top of the WCR averaging domains, seen in Fig. 6b and 6d, were~~
 634 ~~calculated.~~

635 The HP measurements were averaged over two adjacent 60 s intervals. The first extends
 636 from t_0 to $t_0 + 60$ s (Fig. 6a) and the second from $t_0 + 60$ s to $t_0 + 120$ s (Fig. 6c). In Fig. 6a
 637 and in Fig. 6c, $t_{HP,B}$ symbolizes an interval’s beginning time and $t_{HP,E}$ symbolizes an interval’s
 638 ending time. Formulas describing how these times were related to the beginning and ending time
 639 of a corresponding WCR averaging interval are in the Appendix. Fig. 6b is a schematic of the
 640 first WCR averaging interval and Fig. 6d is a schematic of the second. Again, the subscripts “B”
 641 and “E” are used to indicate averaging beginning and ending times. Figures 6b and 6d both have
 642 lines at the top of an averaging interval/domain. The slopes of these lines are proportional to the
 643 ratio of two speeds. These speeds are a maximum likely snow particle speed toward the ground (

644 v_p) and a horizontal wind advection speed (v_w). The v_p was calculated using averaged vertical-
645 component Doppler velocities and v_w was calculated using a vertical profile of horizontal winds,
646 based on WKA horizontal wind measurements and AF horizontal wind measurements (Figs.
647 A1a-b), and using the WKA track vector (Table 2). An altitude ($z' = 3400$ m) was assumed in the
648 calculation of v_w . This is the altitude of the ridges west and northwest of the HP site (Figs. 3a-b).
649 Picking the altitude to be either $z' = 3200$ m or $z' = 3600$ m does not alter our findings.

650

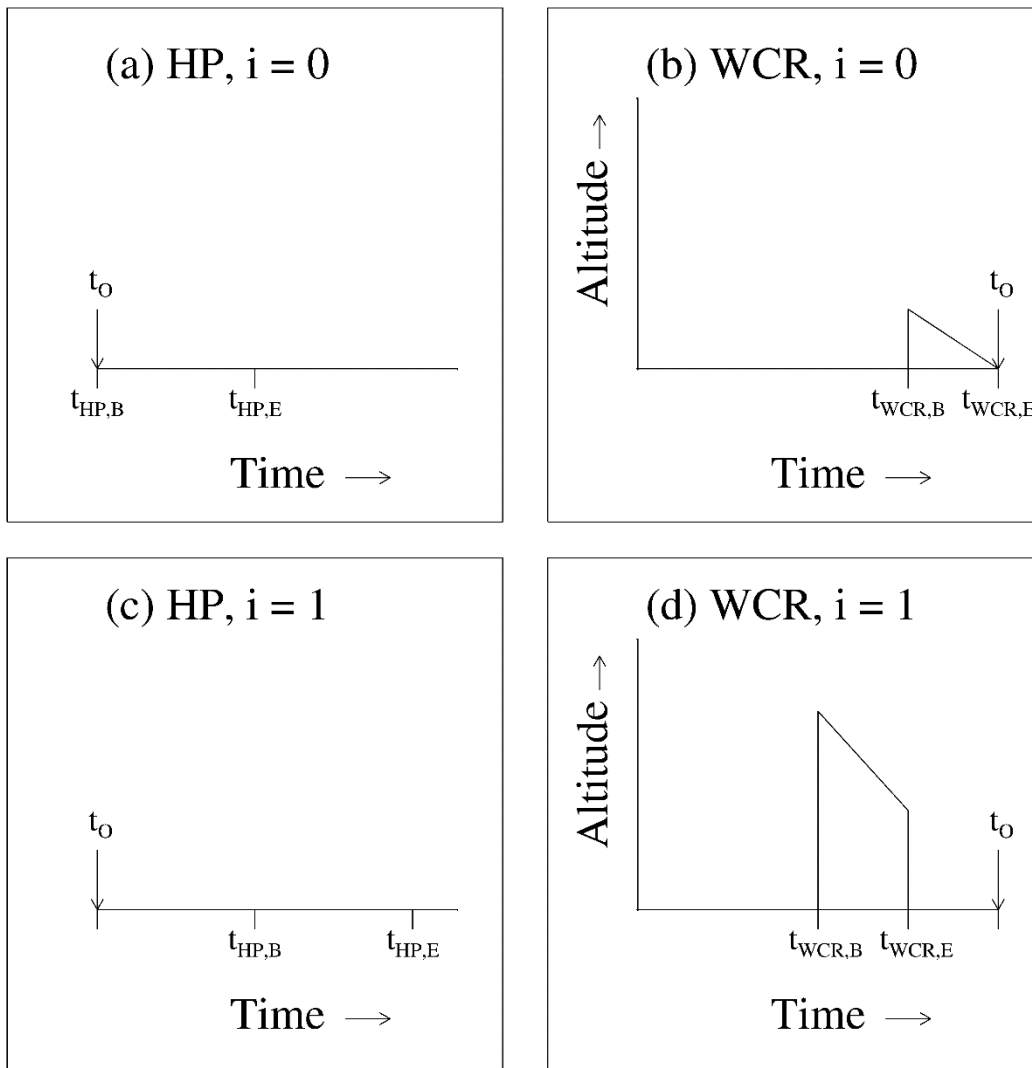
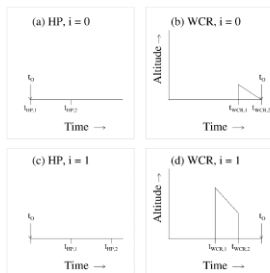


Figure 6 – (a and c) Representations of the $i = 0$ and $i = 1$ HP averaging intervals. (b and d) Representations of the $i = 0$ and $i = 1$ WCR averaging intervals/domains. The t_0 is shown in all panels. The subscripts “B” and “E” indicate beginning and ending times of HP averaging (panels a and c) and the beginning and ending times of WCR averaging (panels b and d).

688 All panels in Fig. 6 are labeled with an index designating either the first averaging
689 interval ($i = 0$) or the second averaging interval ($i = 1$). Figures 7 and 8 present hotplate
690 snowfall measurements from 14/15 December 2016 and 3 January 2017. In these, and in
691 subsequent figures, colored circles surround the indexes, blue is used to color-code 15 December
692 2016, and red is used to color-code 3 January 2017.

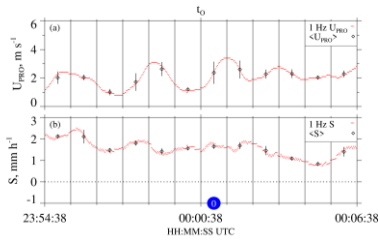
693 Figure 9a and Fig. 10a have enlarged views of the altitude-time crosssections ~~reflectivity~~
694 ~~structures~~ recorded on the two flight days. Different from Fig. 5a and Fig. 5c, these
695 measurements are only from the WCR's down-looking antenna. Additional differences are the
696 following: 1) The plots are set up so that Z and V_D structures downwind of the hotplate can be
697 seen. These structures are discussed in the following section. 2) The WCR measurements are
698 shown for 50 s of flight. With the WKA ground speed approximately 125 m s^{-1} (Table 2), the
699 distance along the abscissa is 6250 m. 3) Colored circles that surround the $i = 0$ index are placed
700 below the WCR averaging intervals/domains ~~(reflectivity and Doppler velocity)~~. The latter
701 ~~domains~~ are drawn with solid black lines and ~~these~~ are seen to overlay ~~both the Z data (Fig. 9a~~
702 ~~and Fig. 10a) and the V_D data (Fig. 9b and Fig. 10b)~~. ~~both the Z and V_D altitude-time~~
703 ~~crosssections~~. Consistent with Figs. 6b and 6d, and the Appendix, one of these black lines is
704 vertical and the other is negatively sloped.

705



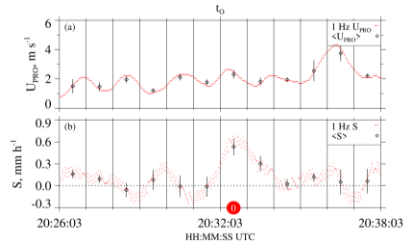
THE REVISED FIGURE IS ABOVE.

Figure 6—(a and c) Schematic diagrams of the $i=0$ and $i=1$ one minute HP averaging intervals. (b and d) Schematic diagrams of the $i=0$ and $i=1$ WCR averaging domains with the lowest retrievable weather target at the low end of the ordinate. The t_0 is shown in all panels.



THE REVISED FIGURE IS BELOW.

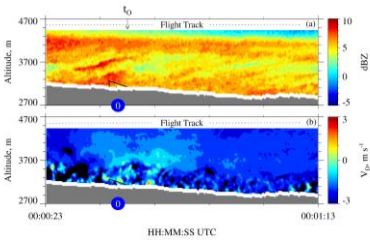
Figure 7—Twelve minutes of hotplate data from 14/15 December 2016. (a) Wind speed. (b) Snowfall rate. In (a), red dots are the one minute running average U_{pro} , recorded at 1 Hz, and in (b), red dots are values of S computed using hotplate output recorded at 1 Hz. In both panels the black diamonds are the one minute averaged values (± 1 standard deviation). The t_0 is shown above the top panel and the large blue circle indicates the $i=0$ HP averaging interval.



THE REVISED FIGURE IS BELOW.

Figure 8—Twelve minutes of hotplate data from 3 January 2017. (a) Wind speed. (b) Snowfall rate. In (a), red dots are the one minute running average U_{PRO} , recorded at 1 Hz, and in (b) red dots are values of S computed using hotplate output recorded at 1 Hz. In both panels the black diamonds are the one minute averaged values (± 1 standard deviation). The t_0 is shown above the top panel and the large red circle indicates the $i=0$ HP averaging interval.

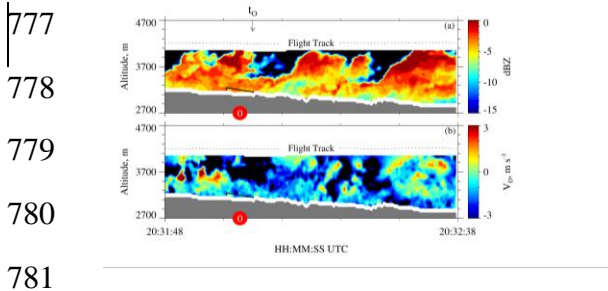
760
761
762
763
764



765 THE REVISED FIGURE IS BELOW.

766
767
768
769
770

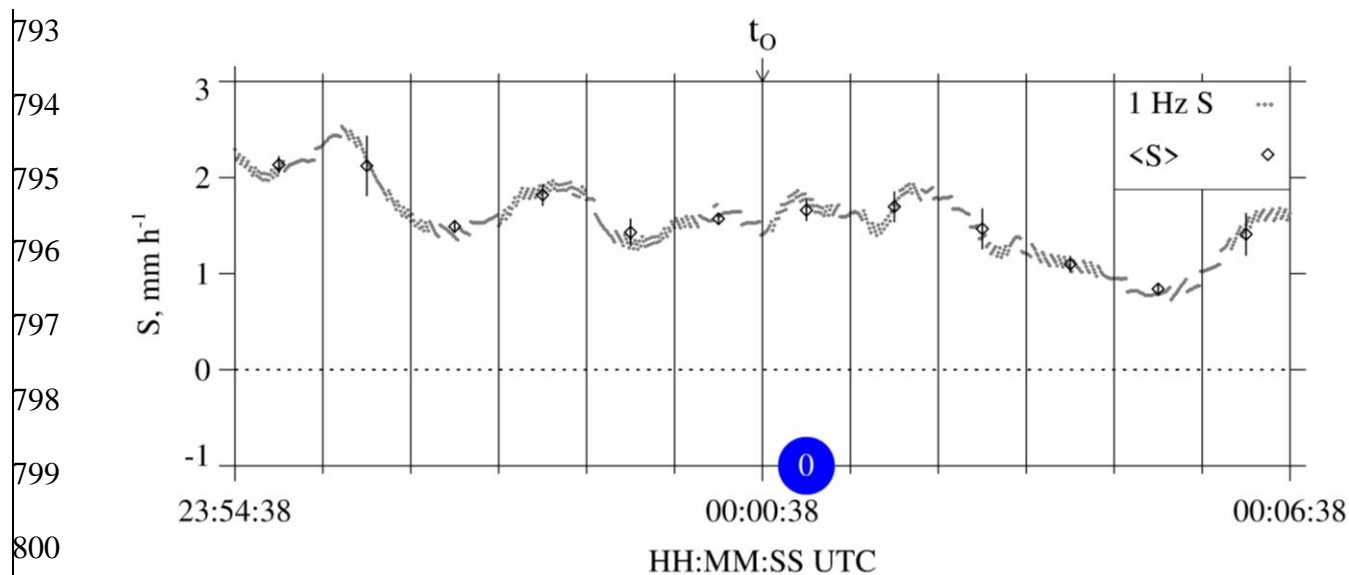
771 ~~Figure 9—50 s of measurements from the down looking WCR antenna on 15 December 2016.~~
 772 ~~(a) Crossection of reflectivity $t_0 - 15$ s to $t_0 + 35$ s. (b) Crossection of Doppler velocity $t_0 - 15$~~
 773 ~~s to $t_0 + 35$ s. The t_0 is shown above the top panel. In both panels, the solid black lines (vertical~~
 774 ~~and sloped) encompass the $i = 0$ WCR averaging domain and the blue circles have the $i = 0$~~
 775 ~~index.~~
 776



THE REVISED FIGURE IS BELOW.

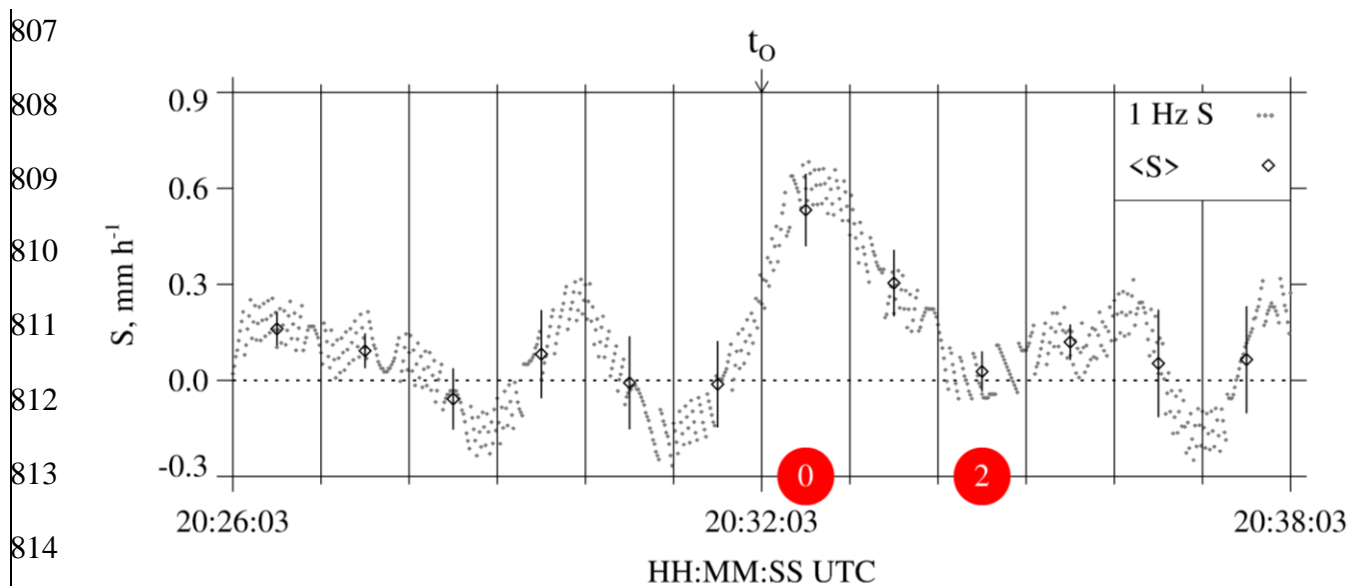
788 ~~Figure 10—50 s of measurements from the down-looking WCR antenna on 3 January 2017. (a)~~
 789 ~~Crosssection of reflectivity $t_0 - 15$ s to $t_0 + 35$ s. (b) Crosssection of Doppler velocity $t_0 - 15$ s to~~
 790 ~~$t_0 + 35$ s. The t_0 is shown above the top panel. In both panels, the solid black lines (vertical and~~
 791 ~~sloped) encompass the $i = 0$ WCR averaging domain and the red circles have the $i = 0$ index.~~

792



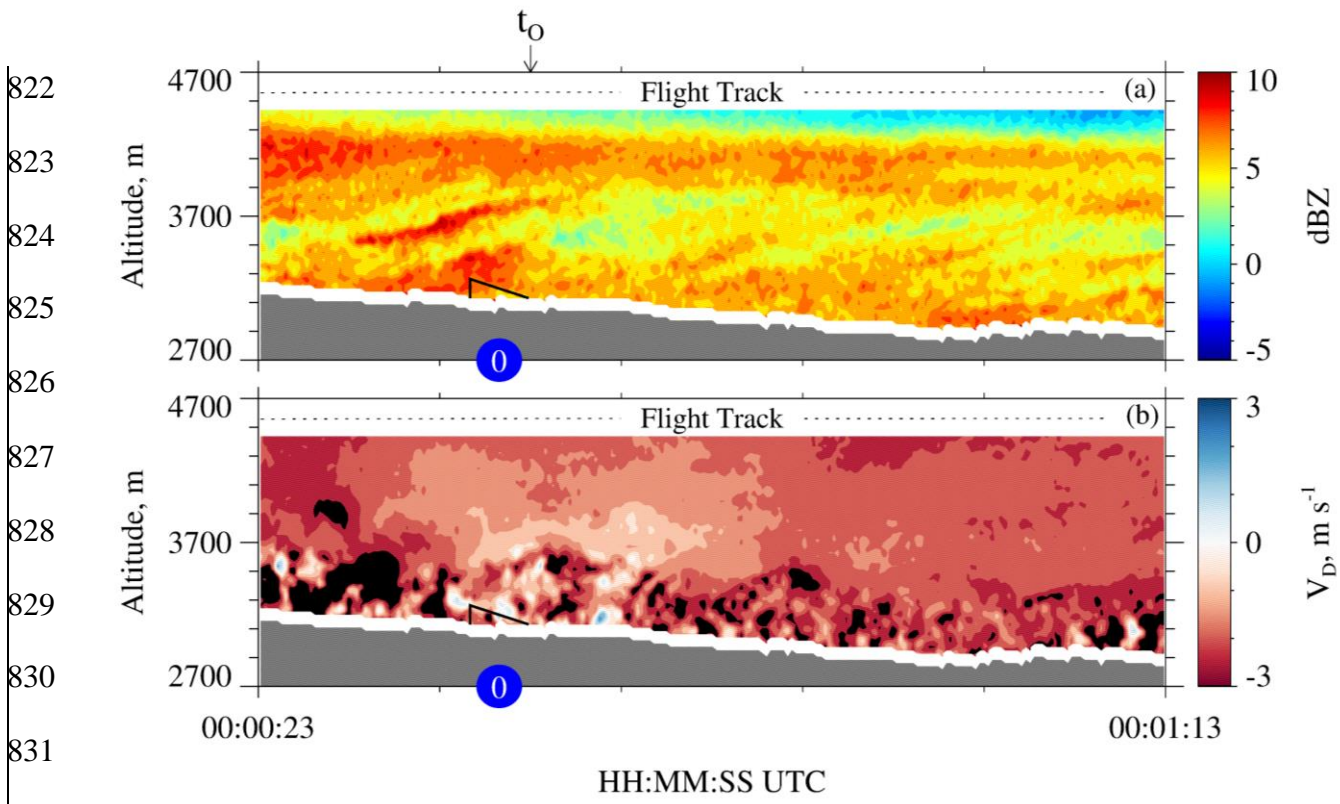
802 Figure 7 – Twelve minutes of HP snowfall measurements from 14/15 December 2016. Gray dots
 803 are S values calculated using hotplate output recorded at 1 Hz. Black diamonds are the one-
 804 minute-averaged values (± 1 standard deviation). The t_0 is shown above the panel and the blue
 805 circle designates the $i = 0$ HP averaging interval.

806



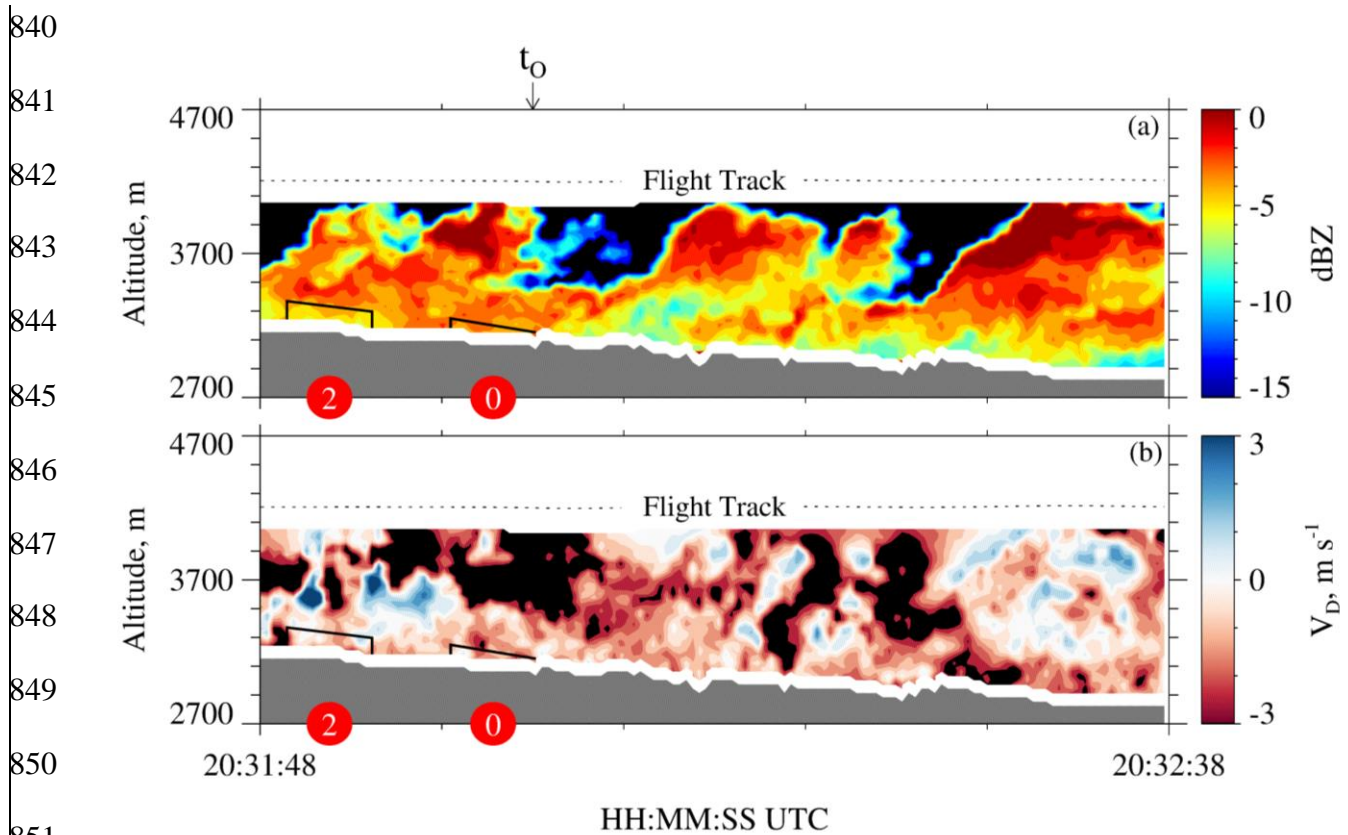
817 Figure 8 – Twelve minutes of HP snowfall measurements from 3 January 2017. Gray dots are S
 818 values calculated using hotplate output recorded at 1 Hz. Black diamonds are the one-minute-
 819 averaged values (± 1 standard deviation). The t_0 is shown above the panel, a red circle designates
 820 the $i = 0$ HP averaging interval, and a red circle designates the $i = 2$ HP averaging interval.

821



834 Figure 9 – 50 s of measurements from the down-looking WCR antenna on 15 December 2016.
835 (a) Crossection of reflectivity $t_0 - 15$ s to $t_0 + 35$ s. (b) Crossection of Doppler velocity $t_0 - 15$ s
836 to $t_0 + 35$ s. The t_0 is shown above the top panel. In both panels, the solid black lines (vertical
837 and sloped) encompass the $i = 0$ WCR averaging interval/domain and blue circles designate the
838 $i = 0$ WCR averaging interval.

839



853 Figure 10 – 50 s of measurements from the down-looking WCR antenna on 3 January 2017. (a)
 854 Cross-section of reflectivity $t_0 - 15$ s to $t_0 + 35$ s. (b) Cross-section of Doppler velocity $t_0 - 15$ s to
 855 $t_0 + 35$ s. The t_0 is shown above the top panel. In both panels, the solid black lines (vertical and
 856 sloped) encompass the $i = 0$ and $i = 2$ WCR averaging intervals/domains, two red circles
 857 designate the $i = 0$ WCR averaging interval, and two red circles designate the $i = 2$ WCR
 858 averaging interval.

859

860 The $i = 0$ averages of S and Z are presented in Table 54 and the corresponding averaging
861 intervals/~~domains~~ are viewable in Fig. 7b and Fig. 9a (15 December 2016) and in Fig. 8b and
862 Fig. 10a (3 January 2017). The $i = 1$ averages are also presented in Table 54. According to the
863 averaging scheme (Fig. 6), the $i = 1$ HP averaging interval is time-shifted positively compared to
864 the $i = 0$ HP averaging interval and the $i = 1$ WCR averaging domain is time-shifted negatively
865 compared of the $i = 0$ WCR averaging ~~interval~~domain. This arrangement of the averaging
866 intervals/~~domains~~ is one way to average while also accounting for wind advection of the snow
867 particles.

868 As discussed earlier in this section, the averaging scheme initializes with 60-second
869 blocks of HP data between t_o and $t_o + 120$ s. When we applied the scheme to data from 3
870 January 2017, but outside the specified time range, an inconsistency was documented. This is
871 apparent in Fig. 8, where the $t_o + 120$ s to $t_o + 180$ s interval (i.e., the $i = 2$ interval) has negligible
872 average S, while in Fig. 10, the $i = 2$ interval has a non-negligible average Z ($\sim 0.3 \text{ mm}^6 \text{ m}^{-3}$). A
873 firm explanation is not available for the inconsistency, but a factor may be the convective nature
874 of the fields in Figs. 10a-b. Because of the inconsistency, only averages corresponding to the
875 $i = 0$ and $i = 1$ intervals were analyzed further.

876

877 Table 54 – Averaged wind, hotplate, and WCR measurements

Date	v_w^a , m s ⁻¹	i index	$\langle S \rangle \pm \sigma_S^b$, mm h ⁻¹	WCR Samples ^c	$\langle V_D \rangle^d$, m s ⁻¹	$\sigma_{V_D}^e$, m s ⁻¹	v_p^f , m s ⁻¹	$\langle Z \rangle \pm \sigma_Z^g$, mm ⁶ m ⁻³
15 December 2016	7.4	0	1.7±0.1	42	-1.3	0.9	2.2	4.9±2.1
15 December 2016	7.4	1	1.7±0.2	149	-1.8	1.2	3.0	5.6±1.1
3 January 2017	8.9	0	0.5±0.1	20	-0.8	0.8	1.6	0.49±0.05
3 January 2017	8.9	1	0.3±0.1	35	-0.8	0.4	1.2	0.50±0.10

878

879 ^a Horizontal wind advection speed (Eq. A75) calculated using values from the penultimate and last
880 columns of Table 2.

881

882 ^b One-minute average of the undercatch-corrected liquid-equivalent snowfall rate (± 1 standard deviation).

883 Example averaging intervals are the $i = 0$ intervals in Fig. 7.b and Fig. 8b.

884

885 ^c Number of samples used to calculate WCR statistics in the penultimate four columns. The averaging
886 domains (e.g., the $i = 0$ domains in Figs. 9a-b and 10a-b) encompass the averaged WCR samples.

887

888 ^d Average of Doppler velocity within the averaging intervals/domains.

889

890 ^e Standard deviation of Doppler velocity within the averaging intervals/domains.

891

892 ^f Maximum likely snow particle speed toward the surface (Eq. A86).

893

894 ^g Average reflectivity (± 1 standard deviation). These values are not corrected for attenuation.

895

896 3.65 - Snow Particle Imagery

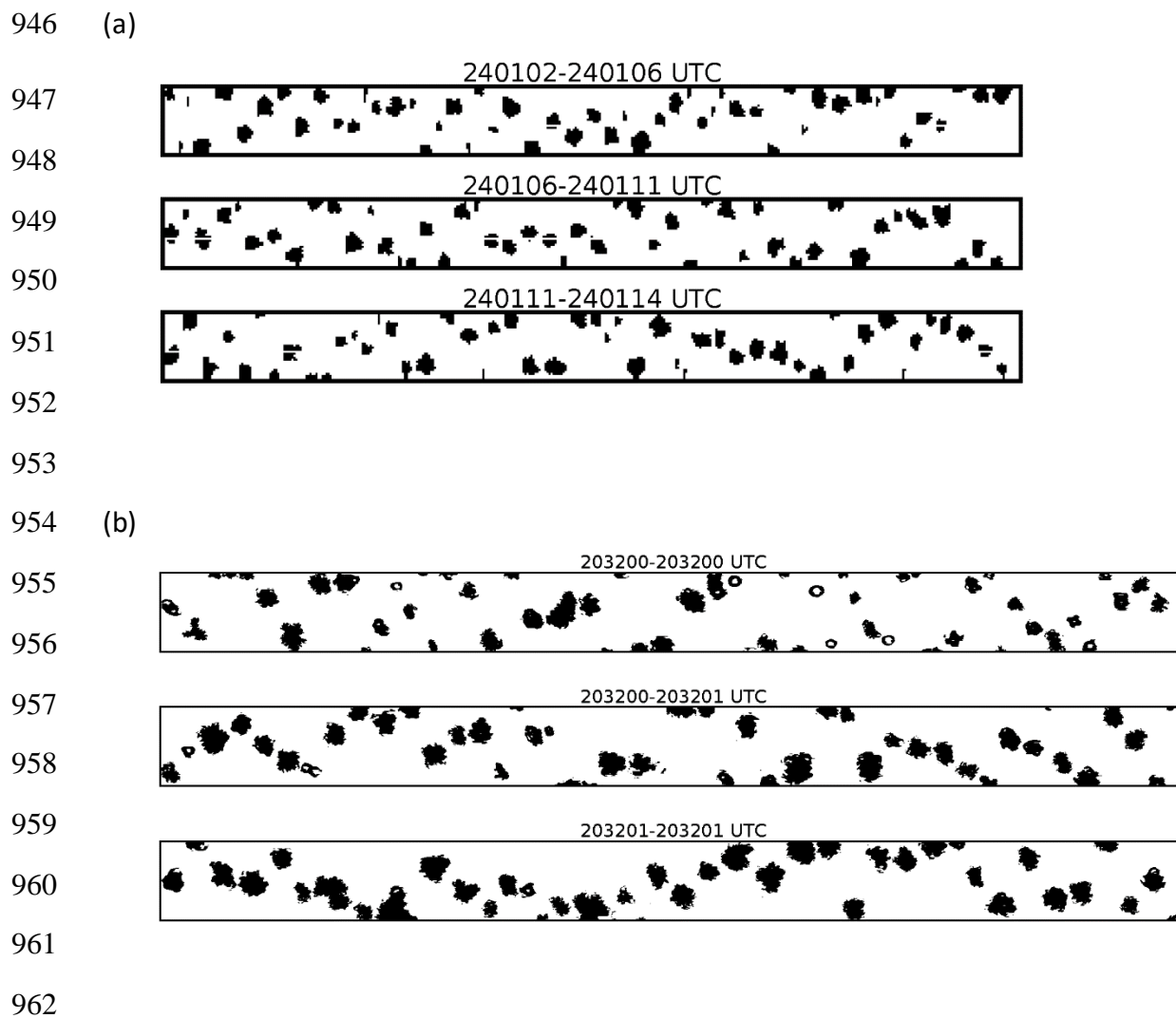
897 In Fig. 9a and Fig. 10a, the time for a snow particle to move the abscissa and ordinate
 898 distances is different. The ratio of these two times is 2.6. This follows from our choice of
 899 abscissa and ordinate ranges, from values of particle fall speed (1 m s^{-1}) and horizontal wind
 900 advection speed (8 m s^{-1}), which we assumed, and from the WKA ground speed ($g_s \sim 125 \text{ m s}^{-1}$;
 901 Table 2). The assumed values are approximately consistent with values of $\langle V_D \rangle$ and v_w , in
 902 Table 54, and with the V_D sign convention (Sect. 2.3). We used $g_s = 125 \text{ m s}^{-1}$ to scale
 903 (virtually) the time axes in Fig. 9a and Fig. 10a to a horizontal distance. Within the scaled
 904 coordinate frames, we assumed that all snow particle trajectories have negative slope ($\Delta z / \Delta x = -$
 905 $1 \text{ m s}^{-1} / 8 \text{ m s}^{-1} = -0.12$) and that all trajectories are stationary. However, both assumptions seem
 906 inconsistent with the reflectivity structures in Fig. 5a, where positively-sloped particle fall
 907 streaks are evident at $\sim 5500 \text{ m}$, inconsistent with Fig. 9a where positively-sloped fall streaks are
 908 at $\sim 3500 \text{ m}$, and inconsistent with the positively-sloped fall streaks in Fig. 10a. On both flight
 909 days, the fall streaks evince particle sources that move horizontally and with a horizontal speed
 910 that is larger than the $v_w = 8 \text{ m s}^{-1}$ we applied in ~~the our~~ estimate of the trajectory slope ~~and in our~~
 911 ~~evaluation of the WCR averaging domains (Sect. 3.4)~~. It may be that the source's horizontal
 912 speed is comparable to the flight-level WKA-derived horizontal wind (27 to 32 m s^{-1} ; Table 2)
 913 but we do not have data needed to verify that assertion. Based on our qualitative interpretation of
 914 the fall streaks, and the assumption that snow particles followed the fall streaks while both were
 915 advecting horizontally, we looked *downwind* of the hotplate - at a time later than t_O in Fig. 9a
 916 and Fig. 10a - for particles that became those that produced snowfall at the hotplate.

917 Particle images from 15 December 2016 were analyzed using the 2DP. With this
918 instrument the maximum all-in particle size (~~in~~ in the horizontal direction perpendicular to flight),
919 is 6400 μm and the particle size resolution is 200 μm (Sect. 2.2). Within the time interval we
920 picked for this analysis (discussed below), particles sizing in the smaller of the two spectral
921 modes, with mode size $\sim 400 \mu\text{m}$, were more numerous (results not shown). Because the 400 μm
922 particles are poorly resolved by the 2DP, and the same can be said for somewhat larger particles,
923 those smaller than 1000 μm were excluded from the following analysis. Figure 11a shows
924 imagery from 12 s of measurements acquired near the end of the sequence in Fig. 9a (00:01:02 to
925 00:01:14). This time interval was selected by tracing ~~backwards~~-forward from t_o , along the
926 slope of the fall streaks in Fig. 9a, to the flight level. Many of the particles are rounded
927 (indicating riming) and a few have arms likely due to incomplete conversion of branched crystals
928 to rimed snow particles. The mode size corresponding to these images is 1600 μm . No liquid
929 water was detected with these particles ($\text{LWC} < 0.01 \times 10^{-3} \text{ kg m}^{-3}$; Fuller 2020; her Figure 8), but
930 liquid was detected, at $\sim 00:00:00$, as the aircraft approached the ridgeline (~~Sect. 3.4~~ Figs. 5a-b).

931 Turning to imagery from 3 January 2017, the most appropriate location for analysis
932 would be through the second billow structure evident in Fig. 10a. This billow sourced a fall
933 streak that terminated at the hotplate (i.e., at the time t_o indicated in the figure). However, the
934 aircraft only clipped the top of this billow, and it was only when sampling the billow seen ~ 13 s
935 earlier that larger ice particle concentrations ($\sim 20,000 \text{ m}^{-3}$) (Fuller 2020; her Figure 10) and
936 larger LWC (~~> 0.06~~ $\sim 0.08 \times 10^{-3} \text{ kg m}^{-3}$; Fig. 5d) were detected. Maximum reflectivities were the
937 same in all three billows ($Z \sim 1 \text{ mm}^6 \text{ m}^{-3}$; 0 dBZ), so we assumed that imagery collected in the
938 first billow (20:32:00 to 20:32:02) was representative of what was falling toward the hotplate.
939 The 2DS was used to image these particles (Fig. 11b); with this instrument the maximum all-in

940 particle size (in the horizontal direction perpendicular to flight), is 1280 μm and the size
941 resolution is 10 μm (Sect. 2.2). Most of the objects in Fig. 11b appear to be rimed and their mode
942 size is $\sim 400 \mu\text{m}$. It is also noted that we eliminated particles smaller than 100 μm from these
943 images, however, compared to the $\sim 400 \mu\text{m}$ particles those smaller than 100 μm were
944 significantly less abundant (results not shown).

945



963 Figure 11 – (a) 2DP particle imagery from 15 December 2016. The height of the strips is 6400
964 μm . These particles are estimated to be representative of those that fell from flight level toward
965 the hotplate. (b) 2DS particle imagery from 3 January 2017. The height of the strips is 1280 μm .
966 These particles are estimated to be representative of those that fell from flight level toward the
967 hotplate.

968

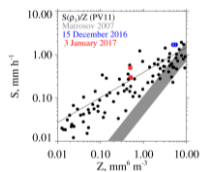
969 **3.76 – S/Z Relationships**

970 ~~The S/Z pairs presented by PV11 in their Figure 11 vary by a factor of ten about their~~
971 ~~best fit relationship ($S(\rho_+)/Z$). Those results are shown in Fig. 12 with black circles and a black~~
972 ~~line. Our S/Z pairs are presented in Table 4 and are plotted in Fig. 12 where we used the indexes~~
973 ~~($i=0$ and $i=1$) to indicate the averaging intervals/domains. Our data pairs plot above the~~
974 ~~$S(\rho_+)/Z$ relationship but within the variability.~~

975 Our S/Z pairs are presented in Table 5 where the indexes ($i = 0$ and $i = 1$) are used to
976 indicate results derived for the averaging intervals. Here, the reflectivities are not corrected for
977 attenuation, however, in Fig. 12, the attenuation-corrected reflectivities are plotted. Uncorrected-
978 reflectivities from Table 5, attenuations from Table 3, and Eq. 1 were used to calculate the
979 corrected reflectivities. Also shown is a subset of the S/Z pairs from PV11's Fig. 11 ($0.01 < Z <$
980 $10 \text{ mm}^6 \text{ mm}^{-3}$) and the PV11 best-fit line (black). In the figure legend, results from PV11 are
981 specified as $S(\rho_+)/Z$ because those authors applied the lower of two density-size functions (ρ_1)
982 with airborne measurements of optical particle images to calculate the snowfall rates (Sect. 1).
983 Our data pairs plot above the $S(\rho_+)/Z$ line but within the variability of PV11's measurements.

984

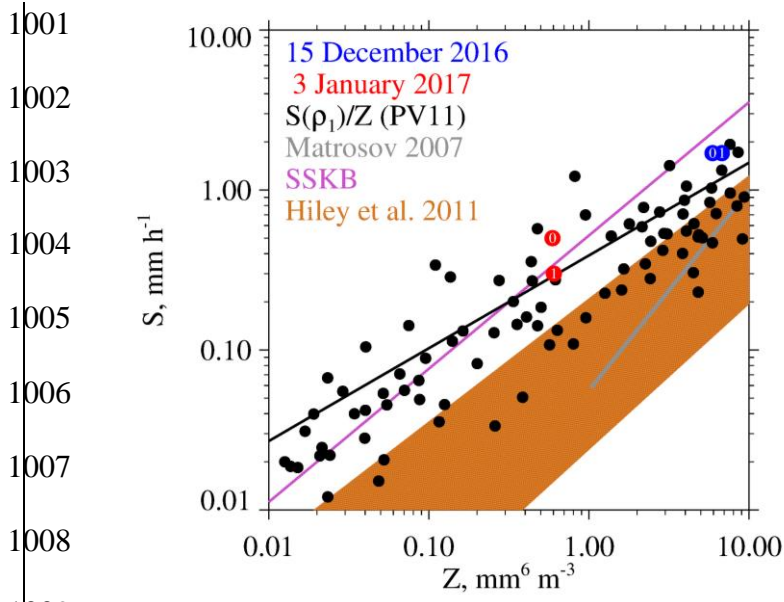
985



986
987
988
989
990 THE REVISED FIGURE IS BELOW.
991
992
993
994
995

996 ~~Figure 12— Snowfall rate (S) versus radar reflectivity (Z). The $S(\rho_+)$ / Z data points are from~~
997 ~~PV11 (their Figure 11). The $S(\rho_+)$ / Z relationship and the upper and lower limit Matrosov~~
998 ~~(2007) S/Z relationships are presented as math functions in Sect. 1. Results for $i=0$ and $i=1$~~
999 ~~averaging intervals/domains are shown with colored circles.~~

1000



1010 Figure 12 – Snowfall rate versus radar reflectivity. Colored circles indicate attenuation-corrected
 1011 reflectivities (Table 3, Table 5, and Eq. 1) for the $i = 0$ and $i = 1$ averaging intervals. The $S(\rho_1)/Z$
 1012 points are a subset from PV11’s Fig. 11 ($0.01 < Z < 10 \text{ mm}^6 \text{ mm}^{-3}$). Also plotted is the PV11
 1013 best-fit line (black), the S/Z relationship from Matrosov (2007), the S/Z relationship abbreviated
 1014 SSKB (Sect. 1), and the swath of S/Z relationships, for crystals, from Hiley et al. (2011).

1015

1016 There are two potential biases in the values of S we tabulate (Table 54) and plot (Fig. 12).
1017 First, the two snowfall events had flight-level vertical wind velocities that were positive
1018 (upward) upwind of the summit, and vice versa downwind of the summit. Except for the
1019 strongest downdraft on 3 January 2017, the magnitude of this variance is $\sim 1 \text{ m s}^{-1}$ (Figs. 5b and
1020 5d). Assuming 1 m s^{-1} was the downward wind immediately over the hotplate, the snow particles
1021 would have approached the gauge faster than their fall speed, and especially so on 3 January
1022 2017. Our basis for stating this is fall speeds for the mode sizes discussed in Sect. 3.6 (1600 and
1023 400 μm) and our assumption that the particles were graupel-(~~Table 5~~). (Table 6 has these
1024 characteristic sizes and fall speeds.) However, the conjectured downdraft speed is likely an
1025 overestimate - because of divergence occurring as the draft approached the surface - and because
1026 the sizes in Table 65 likely underestimate what fell to the hotplate. Relevant to the last of these
1027 assertions, we used the T/RH/altitude measurements (Table 2) to calculate the vertical distance
1028 available for growth via riming, and thus for a fall speed increase, between the flight level and
1029 the lifted condensation level. Assuming an adiabatically-stratified supercooled cloud and unit
1030 collection efficiency (these assumptions overestimates growth by riming), and no change of
1031 particle crosssection (underestimates growth by riming), our calculations indicate that relative
1032 increases of size and fall speed were 40 and 20 %, respectively, on 3 January 2017, and that
1033 these relative increases were a factor-of-two larger on 15 December 2016.

1034

1035 Table 65 – Estimates of snow particle fall speed

Date	Mode Size, μm	Assumed Particle Type	Fall Speed, m s^{-1}	Reference
15 December 2015	1600	graupel	1.4	PV11; assuming ρ_1 in their Figure 5
3 January 2016	400	graupel	0.7	PV11; assuming ρ_1 in their Figure 5

1036
1037

1038 Second, there is concern that values of S from 3 January 2017 are underestimated.

1039 Although, values of S must be > 0 , we presented 1 Hz values (red points, Fig. 8b) as small as -
1040 0.3 mm h^{-1} . Negative values resulted because we did not impose a threshold of 0 mm h^{-1} on the
1041 uncorrected snowfall rates (this thresholding is discussed in Z18) and because negative snowfall
1042 rate values (uncorrected for catch inefficiency) are amplified by the gauge-catch correction (Sect.
1043 2.4). The implication is that 0.2 mm h^{-1} could be added to the one-minute averaged values of S in
1044 Table 54 and in Fig. 12. Here, the assumption is that an averaged S of -0.2 mm h^{-1} , in Fig. 8b, is
1045 indicating no snowfall ~~at the hotplate and no surface deposition of blowing snow~~; however,
1046 because the hotplate was operated autonomously (Sect. 2.1) we have no way to verify the
1047 assumption.

1048 **4 – Results**

1049 ~~Our paired values of surface measured precipitation and aircraft measured radar~~
1050 ~~reflectivity provide evidence in addition to PV11 that most prior determinations of the S/Z~~
1051 ~~relationship for W band radars lead to underestimation of S in situations with rimed snow~~
1052 ~~particles and particularly so in situations with Z smaller than $1 \text{ mm}^6 \text{ m}^{-3}$. We assert that the~~
1053 ~~underestimate stems from the smaller density implicit in most computationally based S/Z~~
1054 ~~relationships and especially those which assume that snow particles consist of vapor grown~~
1055 ~~crystals or aggregates of vapor grown crystals. Values of density are quite different for these two~~
1056 ~~particle types versus that for rimed snow particles. For example, in Matrosov (2007), assuming a~~
1057 ~~2 mm aggregate, the density is $\sim 30 \text{ kg m}^{-3}$, whereas in PV11, assuming a 2 mm graupel particle,~~
1058 ~~the density is $\sim 200 \text{ kg m}^{-3}$.~~

1059 Figure 12 shows our S/Z measurements after we corrected the reflectivities for
1060 attenuation. Below we compare our S/Z measurements to calculations reported by Hiley et al.
1061 (2011), but first, we consider the computational S/Z relationship reported by Matrosov (2007)
1062 and its relevance to our measurements. Since the particle images (Figs. 11a-b) reveal no
1063 compelling evidence for the aggregates modeled by Matrosov (2007), a model based on that
1064 particle type is not a useful comparator. Moreover, the overlap of PV 11's S/Z measurements and
1065 Matrosov's S/Z calculations has already been discussed in the literature (PV11). However,
1066 before going forward, two clarifications will be made about PV11's data points in Fig. 12: 1)
1067 Presentation clarity was what guided our selection of the S and Z axis ranges in this figure but
1068 with the consequence that 32 of PV11's S/Z pairs are not shown at $Z > 10 \text{ mm}^6 \text{ m}^{-3}$. 2) The
1069 scatter of PV11 data at the largest values of Z in Fig. 12, combined with the fact that PV11
1070 points at $Z > 10 \text{ mm}^6 \text{ m}^{-3}$ are not shown, could lead to the interpretation that the slope describing

1071 the relationship at Z approximately $> 2 \text{ mm}^6 \text{ m}^{-3}$ should be decreased relative to the slope of the
1072 PV11 best-fit line. Readers who view PV11's Fig. 11 will conclude that this interpretation is not
1073 warranted.

1074 Calculated S/Z relationships have inputs from parameterized descriptions of density,
1075 shape, fall speed, and PSD. The analysis conducted by Hiley et al. (2011) is the most
1076 comprehensive in this regard, and except for the one aggregate particle type those authors
1077 considered, out of 20 total, they modeled ensembles of crystals. Additionally, Hiley et al. (2011)
1078 did not model ensembles of spherical snow particles. The latter were modeled by Surussavadee
1079 and Staelin (2007) and Kulie and Bennartz (2009), and in Fig. 12 we are using SSKB to
1080 symbolize that computational approach (Sect. 1).

1081 ~~In the previous paragraph, a cutoff at $Z = 1 \text{ mm}^6 \text{ m}^{-3}$ was specified because that is where~~
1082 ~~the separation between the Matrosov (2007) and both our and PV11's WCR observations~~
1083 ~~become evident (Fig. 12). The cutoff was also picked because Kulie et al. (2016) apply it in an~~
1084 ~~analysis of snowfall retrieved using the W-band radar on CloudSat. They concluded that 74% of~~
1085 ~~shallow cumuliform cloud structures, and 37% of nimbostratus cloud structures, have near-~~
1086 ~~surface reflectivities $< 1 \text{ mm}^6 \text{ m}^{-3}$. Depending on which snowfall process dominates in these~~
1087 ~~structures (vapor growth, aggregation, or riming) an alteration of S for $Z < 1 \text{ mm}^6 \text{ m}^{-3}$ (e.g., Fig.~~
1088 ~~12) could have a significant effect on W-band retrievals. For example, the analysis of Kulie et al.~~
1089 ~~2016 (their Figure 6) suggests that the Greenland, Norwegian, and Barents Seas regions may be~~
1090 ~~susceptible to this alteration.~~

1091 ~~Some computationally based S/Z relationships (Surussavadee and Staelin (2006) and~~
1092 ~~Kulie and Bennartz (2009)) do plot between PV11's $S(\rho_1)/Z$ relationship—the black line in Fig.~~
1093 ~~12—and Matrosov's upper limit S/Z relationship (the top of the gray area in Fig. 12). Of these~~

1094 ~~the Surussavadee and Staelin relationship assumes that the snow particles are spheres. This~~
1095 ~~seems reasonable for rimed snow particles but not for the crystal and aggregate types modeled by~~
1096 ~~Matrosov (2007) where the particles are approximated as low density oblate spheroids with their~~
1097 ~~major axis (on average) oriented horizontal. Because of this, proposed space based platforms~~
1098 ~~may carry instrumentation that can guide selection of a scene appropriate S/Z relationship. Both~~
1099 ~~lidar and radiometers can sense supercooled liquid water from space, and if combined with~~
1100 ~~Doppler radar, can diagnose precipitation attributable to rimed snow particles. These approaches~~
1101 ~~are being tested in ground based field studies (Moisseev et al. 2017; Mason et al. 2018).~~

1102 Departures between our S measurements (Fig. 12) and S/Z calculations from Hiley et al.
1103 (2011) were evaluated as the vertical distance between the top of the orange region and our S/Z
1104 data points. Reflectivities at the top of the orange region were calculated using attenuation-
1105 corrected reflectivities (Eq. 1 and Table 5) and the upper-limit S/Z equation from Hiley et al.
1106 (2011) ($S = 0.21 \cdot (Z')^{0.77}$; Sect. 1). The departures were evaluated as a relative difference
1107 expressed as $(S_{HP} - S)/S$ with S_{HP} one of four snowfall rates from Table 5. The relative difference
1108 is no smaller than 0.9 and 1.1 on 15 December and 3 January, respectively. These minimum
1109 relative differences exceed the hotplate precision (Sect. 2.4) by approximately a factor of three.
1110 We therefore conclude that our paired values of surface-measured precipitation rate and aircraft-
1111 measured radar reflectivity, after correcting for attenuation, provide evidence that a calculation
1112 of S based on the Hiley et al. (2011) upper-limit, when applied to rimed snow particles, is
1113 associated with a low-biased estimate of S.

1114

1115

1116 A plausible explanation for the low bias is the smaller density implicit in most
1117 computationally-based S/Z relationships and especially those which assume that snow particles
1118 are crystals. Densities are quite different for crystals versus that for rimed snow particles. For
1119 example, in Kulie and Bennartz (2009; their Eq. 2), assuming a 2 mm crystal, the density is ~ 40
1120 kg m^{-3} , whereas in PV11, assuming a 2 mm graupel particle, the density is $\sim 200 \text{ kg m}^{-3}$. Fig. 12
1121 also has the SSKB relationship. This was developed using density = 200 kg m^{-3} (Sect. 1).
1122 Compared to S/Z relationship represented by top of the orange region in Fig. 12, the SSKB line
1123 plots closer to our data points and closer to most of those reported by PV11.

1124 Our conclusion that the upper-limit S/Z relationship from Hiley et al. (2011)
1125 underestimates S would be modified if the WCR-derived reflectivities were negatively biased.
1126 Assuming the reflectivities are negatively biased by 2.5 dBZ, the minimum relative differences
1127 discussed previously are no smaller than 0.2 and 0.4 on 15 December and 3 January,
1128 respectively. A negative bias of this magnitude cannot be ruled out but neither can a positive
1129 bias of the same magnitude (Sect. 2.3). The latter increases the minimum relative differences to
1130 1.9 and 2.3 on 15 December and 3 January, respectively.

1131 The scatter of measurements in Figure 12, and the plausibility of a -2.5 to +2.5 dBZ bias
1132 in WCR reflectivity measurements, indicate that refined techniques will be needed for future
1133 investigations. Additionally, improved methods are needed to diagnose situations where riming
1134 is occurring within clouds. Both lidars and radiometers can sense supercooled liquid water from
1135 space (e.g., Battaglia and Panegrossi, 2020), and if combined with Doppler radar, can diagnose
1136 precipitation attributable to rimed snow particles. These approaches are being tested in ground-
1137 based field studies (Kneifel et al. 2015; Moisseev et al. 2017; Mason et al. 2018).

1138

1139 5 - Conclusions

1140 This study is significant because it brings together direct measurements of snowfall rate,
1141 measured at the ground, and measurements of reflectivity from an airborne W-band radar.

1142 ~~Compared to PV11's $S(\rho_r)/Z$ relationship, shown in Fig. 12, our observations do not depart~~
1143 ~~significantly; however, they do plot somewhat larger. As shown in Fig. 12, our observations do~~
1144 ~~not depart strongly from the PV11 best-fit line; however, they do plot somewhat larger. This~~
1145 ~~excess could be consistent with downslope flow that occurs in lee of the Medicine Bow~~
1146 ~~Mountains (Sect. 3.6 Figs. 5a and 5d) or with calculations which indicate that larger density is~~
1147 ~~associated with larger S , in the S -versus- Z coordinate system (PV11), combined with the~~
1148 ~~intrinsic variability of the density of rime ice (Macklin 1962).~~

1149 ~~If the downslope flow hypothesis is correct, we expect it to manifest as negatively biased~~
1150 ~~retrievals of S , in settings leeward of a ridgeline, where snowfall is produced by riming, and~~
1151 ~~PV11's $S(\rho_r)/Z$ relationship is applied in the retrieval. This follows because PV11, and all other~~
1152 ~~S/Z relationship developers, do not account for the effect of vertical air motion on S values~~
1153 ~~incorporated into their S/Z relationships. Furthermore, the sign of the hypothesized bias will vary~~
1154 ~~from positive (radar retrieved S larger than a surface measured S) to negative (radar retrieved S~~
1155 ~~smaller than a surface measured S) in the downwind direction across a ridgeline. Finally, we~~
1156 ~~expect the relative magnitude of the hypothesized biases will be enhanced in a situation where Z~~
1157 ~~is measured, snowfall is produced via the diffusion growth of crystals, and the scene appropriate~~
1158 ~~S/Z relationship is applied.~~

1159

1160 If the downslope flow hypothesis is correct, and the PV11 best-fit line is applied to
1161 retrieve S in settings with rimed snow particles, we expect a negatively-biased S retrieval
1162 leeward of a ridgeline, and a positively-biased retrieval windward of a ridgeline. This follows
1163 because PV11 did not account for the effect of vertical air motion on their S/Z relationship,
1164 because of how vertical air motion changes windward to leeward across the Medicine Bow
1165 Mountain ridgeline (Figs. 5b-5d), and because the magnitudes of the windward/leeward vertical
1166 winds are comparable to the downward speed of rimed snow particles in quiescent air. Analysis
1167 of existing data, for example from the SNOWIE project that deployed in western Idaho in 2017
1168 (Tessendorf et al. 2019), could further explore the hypothesis.

1169 New research can also refine the S/Z relationship for rimed snow particles. This could be
1170 computational – exploring the utility of parameterizing S in terms of both Z and density – or
1171 could be observational. Unlike the investigation of PV11, where only an airborne platform was
1172 employed, we have demonstrated how useful information can be obtained with ground-based and
1173 airborne systems. Another approach would be with collocated ground-based instrumentation, for
1174 density and particle imaging, and for measuring wind, snowfall rate, and radar reflectivity. This
1175 would avoid some of the complications encountered in this study, including W-band attenuation
1176 and a reliance on particle imagery acquired aloft. A close-range measuring radar might also
1177 allow retrievals closer to the surface than in this work. Improvement of methods that remotely
1178 sense supercooled cloud water are also needed.

1179

1180

1181 6 - Appendix

1182 ~~This appendix explains how the HP (hotplate) and WCR (Wyoming Cloud Radar)~~
 1183 ~~averages were evaluated.~~

1184 This appendix explains how HP (hotplate) and WCR (Wyoming Cloud Radar) averages
 1185 were evaluated. The scheme starts with an HP averaging interval (duration 60 s) and derives a
 1186 WCR averaging interval and a WCR averaging domain. The latter encompasses a subset of the
 1187 altitude-time crosssection sampled by the WCR. The top boundary of the domain was derived
 1188 using vertical-component Doppler velocities within the interval/domain. Because of this
 1189 dependence, the line defining the top boundary was derived iteratively.

1190 With the overflight time symbolized t_O , ~~and i an index equal to either 0 or 1 the start~~
 1191 ~~and stop times for a one minute HP average are~~ the beginning and ending times of the first of
 1192 two 60-second HP averaging intervals are

$$1193 \quad \del{t_{HP,1} = t_O + i \cdot 60} \quad \del{\hspace{15em}} \quad \del{(A1)}$$

$$1194 \quad t_{HP,B} = t_O \quad (A1)$$

$$1195 \quad t_{HP,E} = t_O + 60 \quad (A2)$$

$$1196 \quad \del{t_{HP,2} = t_O + (i + 1) \cdot 60} \quad \del{\hspace{15em}} \quad \del{(A2)}$$

1197
 1198 ~~Examples of $t_{HP,1}$ and $t_{HP,2}$ are at the left and right edges of the $i=0$ one minute HP averaging~~
 1199 ~~intervals in Fig. 7b and Fig. 8b.~~

1200 ~~The stop time for WCR averaging was calculated as~~

1201 Since two adjacent HP averaging intervals are evaluated in this analysis, we express the
 1202 averaging times with the following recursive equations

1203 ~~$t_{WCR,2} = t_O - i \cdot 60 \cdot v_w / gs.$ (A3)~~

1204 $t_{HP,B}(i) = t_O + i \cdot 60$ (A3)

1205 and

1206 $t_{HP,E}(i) = t_O + (i+1) \cdot 60.$ (A4)

1207 In Eqs. A3-A4 the index is $i \in \{0, 1\}$.

1208 ~~Here v_w is a wind advection speed (discussed below) and the second term on the rhs is a wind~~
 1209 ~~advection distance divided by the WKA (Wyoming King Air) ground speed (gs). The start time~~
 1210 ~~for WCR averaging was calculated as~~

1211 ~~$t_{WCR,1} = t_{WCR,2} - (1+i) \cdot 60 \cdot v_w / gs$ (A4)~~

1212 Analogous to the recursion in Eq. A4, the ending time of a WCR averaging interval is

1213 $t_{WCR,E}(i) = t_O - i \cdot 60 \cdot v_w / gs.$ (A5)

1214 Here v_w is a wind advection speed (discussed below) and the second term on the rhs is a wind
 1215 advection distance divided by the WKA (Wyoming King Air) ground speed (gs). Analogous to
 1216 the Eq. A5, the beginning time of a WCR averaging interval is

1217 $t_{WCR,B}(i) = t_{WCR,E} - (i+1) \cdot 60 \cdot v_w / gs$ (A6)

1218 The wind advection speed (v_w) in Eqs. A53-A64 was calculated using an altitude-
 1219 dependent west-to-east wind velocity (u) and an altitude-dependent south-to-north wind
 1220 velocity (v). These altitude-dependent component velocities were calculated using the horizontal
 1221 wind vectors in the penultimate and last columns of Table 2. Plots of the component velocities
 1222 versus altitude and the linear functions used to relate component velocities to altitude are
 1223 presented in Figs. A1a-b.

~~We assumed an altitude ($z'=3400$ m) for evaluating the horizontal wind advection vector. This is the altitude of the ridges west and northwest of the HP site (Figs. 3a-b). Picking the altitude to be either $z'=3200$ m or $z'=3600$ m does not substantially alter our conclusions.~~

An altitude ($z'=3400$ m) was assumed for evaluating the horizontal wind advection vector. This is the altitude of the ridges west and northwest of the HP site (Figs. 3a-b).

The WKA track vector (Table 2) defines the vertical plane of the WCR measurements. We assumed that wind advection of snow particles occurred parallel to this vector. With the assumption stated in the previous paragraph, the horizontal wind advection speed (v_w) was calculated as the projection of the horizontal wind vector onto the track vector.

$$v_w = \frac{u(z') \cdot g_{s_x} + v(z') \cdot g_{s_y}}{(g_{s_x}^2 + g_{s_y}^2)^{1/2}}. \quad (\text{A75})$$

In Eq. A75 the west-to-east and south-to-north components of the track vector are symbolized g_{s_x} and g_{s_y} . Vector representations of the track vector are in Table 2. On 14/15 December 2016 and 3 January 2017, the values of v_w are 7.4 and 8.9 m s^{-1} , respectively.

In addition to the properties g_s and v_w used to ~~evaluate~~ ~~calculate the averaging times~~ (Eqs. A53-A64), ~~the WCR averages were derived using a snow particle downward speed (Eq. A6).~~ a WCR averaging interval/domain was evaluated using a snow particle downward speed (Eq. A8).

$$v_p = |\langle V_D \rangle| + \sigma_{V_D} \quad (\text{A86})$$

~~Here, v_p is a snow particle downward speed (discussed below), $\langle V_D \rangle$ is the average of Doppler velocities within an averaging domain, $|\langle V_D \rangle|$ is the absolute value of the average,~~

1244 ~~and σ_{V_D} is the standard deviation of the average. On both the lhs and rhs of Eq. A6, all properties~~
 1245 ~~are greater than zero.~~

1246 Here, $\langle V_D \rangle$ is the average of Doppler velocities within an averaging interval/domain, $|\langle V_D \rangle|$
 1247 is the absolute value of the average, and σ_{V_D} is the standard deviation of the average. On both
 1248 the lhs and rhs of Eq. A8, all terms are greater than zero.

1249 We interpret v_p as the maximum likely snow particle speed toward the surface. There are
 1250 three reasons for this: 1) For the WCR averaging intervals/domains we analyzed, values of
 1251 $\langle V_D \rangle$ ~~were~~are consistently less than zero. This indicates that snow particles (on average) were
 1252 moving toward the surface. 2) Again, for the WCR averaging intervals/domains we analyzed,
 1253 σ_{V_D} ~~was~~is comparable to $|\langle V_D \rangle|$. This ~~indicates~~ing that turbulent eddies transported snow
 1254 particles upward and downward at a ~~speeds~~s comparable to their ~~downward fall~~ speed ~~of the snow~~
 1255 ~~particles~~ in quiescent air. 3) The V_D are reflectivity weighted (Haimov and Rodi 2013) and are
 1256 thus indicative of the motion of the largest particles within ~~and averaging interval/domain.~~the
 1257 ~~WCR viewing volume.~~

1258 ~~We now focus on the top of the WCR averaging domains shown schematically in Fig. 6.~~
 1259 ~~The slope defining this upper boundary was calculated as $-v_p - g_s/v_w$. That is, particles below~~
 1260 ~~this boundary were moving downward sufficiently fast and horizontally sufficiently slow to~~
 1261 ~~advect reasonably close to the hotplate. Starting with diagnosed values of g_s and v_w , values of~~
 1262 ~~v_p and thus values of the slope, were derived iteratively. The precision of the derived v_p is ± 0.1~~
 1263 ~~m s^{-1} .~~

1264

1265 We now focus on the top boundary of a WCR averaging interval/domain. Figures 6b and
1266 6d have representations of the boundary. The slope defining this boundary was calculated as
1267 $-v_p \cdot gs / v_w$. That is, particles below this boundary moved downward sufficiently fast and
1268 horizontally sufficiently slow to advect reasonably close to the hotplate. Starting with diagnosed
1269 values of gs and v_w , the values of v_p and slope, were derived iteratively. The precision of the
1270 derived v_p is $\pm 0.1 \text{ m s}^{-1}$.

1271

1272

1273

1274

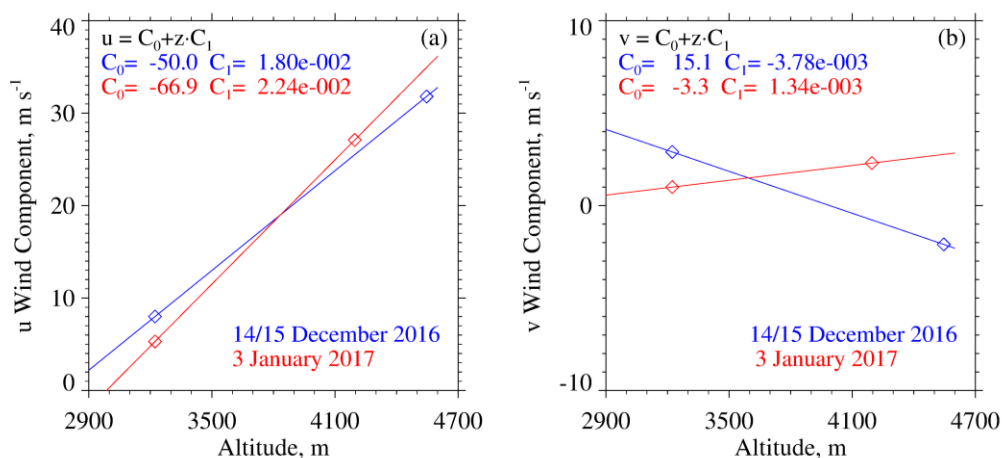
1275

1276

1277

1278

1279



1280 Figure A1 – (a) West-to-east (u) wind velocity derived using measurements from the WKA and

1281 the AmeriFlux (AF) tower. Also shown is the ~~altitude-dependent~~ linear function used to relate u

1282 to altitude. (b) South-to-north (v) wind velocity derived using measurements from the WKA and

1283 AF. Also shown is the ~~altitude-dependent~~ linear function used to relate v to altitude. WKA and

1284 AF velocities are presented as vectors in the penultimate and last columns of Table 2.

1285

1286 Data Availability. The WKA and WCR measurements can be obtained from the SNOWIE data
1287 archive of NCAR/EOL, which is sponsored by the National Science Foundation. Hotplate gauge
1288 measurements are at <https://doi.org/10.15786/20103146>. The US-GLE AmeriFlux measurements
1289 are at <https://ameriflux.lbl.gov/>. The Brooklyn Lake SNOTEL gauge measurements are at
1290 <https://www.wcc.nrcs.usda.gov/snow/>. [Merged Hotplate, SNOTEL, and AmeriFlux data](#)
1291 [sequences from 14/15 December 2016 and 3 January 2017 are in Snider \(2023\).](#)
1292

1293 Author contributions. JRS and MB wrote ~~a successful~~the grant proposal that funded this
1294 research. Field measurements were performed by SF, SM, SH, MB, and JRS. SF wrote her MS
1295 dissertation, and this was adapted for this paper by JRS. KS processed the snow particle imagery.
1296 AM maintained the measurement sites. All authors contributed to the editing of this paper.
1297

1298 **Acknowledgements** –

1299 We acknowledge the expert technical assistance provided by David Plummer, Larry
1300 Oolman, Zane Little, Brent Glover, Edward Sigel, Thomas Drew, and Brett Wadsworth. We
1301 thank SNOWIE project PI Jeffery French, who provided the flight data, Gabor Vali who
1302 provided the S/Z data points in Figure 12, and John Frank and John Korfmacher who acquired
1303 ~~and maintain~~ the GLE-US AmeriFlux data set. This work was supported by the United States
1304 National Science Foundation (Award Number 1850809) and the John P. Ellbogen Foundation.

1305 **References**

- 1306 AmeriFlux, <https://ameriflux.lbl.gov/>, 2021
- 1307 Battaglia, A. and Panegrossi, G., What Can We Learn from the CloudSat Radiometric Mode
1308 Observations of Snowfall over the Ice-Free Ocean?, 12, 3285,
1309 <https://doi.org/10.3390/rs12203285>, 2020
- 1310 Boudala, F.S., R. Rasmussen, G.A. Isaac, and B. Scott, Performance of Hot Plate for Measuring
1311 Solid Precipitation in Complex Terrain during the 2010 Vancouver Winter Olympics, J.
1312 Atmos. Oceanic Technol., 31, 437–446, <https://doi.org/10.1175/JTECH-D-12-00247.1>,
1313 2014
- 1314 Braham , R. R., Snow Particle Size Spectra in Lake Effect Snows. J. Appl. Meteor. Climatol., 29,
1315 200–207, [https://doi.org/10.1175/1520-0450\(1990\)029<0200:SPSSIL>2.0.CO;2](https://doi.org/10.1175/1520-0450(1990)029<0200:SPSSIL>2.0.CO;2), 1990
- 1316 Brock, F. V., and Richardson, S. J., Meteorological Measurement Systems, Oxford University Press,
1317 New York, 304 pp., 2001
- 1318 Cocks, S.B., S.M. Martinaitis, B. Kaney, J. Zhang, and K. Howard, MRMS QPE Performance during
1319 the 2013/14 Cool Season, J. Hydrometeor., 17, 791–810, <https://doi.org/10.1175/JHM-D-15-0095.1>, 2016
- 1321 Faber, S., French, J. R., and Jackson, R., Laboratory and in-flight evaluation of measurement
1322 uncertainties from a commercial Cloud Droplet Probe (CDP), Atmos. Meas. Tech., 11,
1323 3645–3659, <https://doi.org/10.5194/amt-11-3645-2018>, 2018
- 1324 Field, P.R., Hogan, R.J., Brown, P.R.A., Illingworth, A.J., Choulaton, T.W. and Cotton, R.J.,
1325 Parametrization of ice-particle size distributions for mid-latitude stratiform cloud. Q.J.R.
1326 Meteorol. Soc., 131: 1997-2017. <https://doi.org/10.1256/qj.04.134>, 2005
- 1327 Fuller, S.E., Improvement of the Snowfall / Reflectivity Relationship for W-band Radars, MS
1328 Thesis, Department of Atmospheric Science, University of Wyoming, 2020
- 1329 Geerts, B., Q. Miao, Y. Yang, R. Rasmussen, and D. Breed, An Airborne Profiling Radar Study of
1330 the Impact of Glaciogenic Cloud Seeding on Snowfall from Winter Orographic Clouds, J.
1331 Atmos. Sci., 67, 3286–3302, <https://doi.org/10.1175/2010JAS3496.1>, 2010
- 1332 Haimov, S., and Rodi, A., Fixed-Antenna Pointing-Angle Calibration of Airborne Doppler Cloud
1333 Radar, Journal of Atmospheric and Oceanic Technology, 30, 2320-2335,
1334 <https://doi.org/10.1175/JTECH-D-12-00262.1>, 2013
- 1335 Hiley, M. J., M. S. Kulie, and R. Bennartz, Uncertainty Analysis for CloudSat Snowfall Retrievals, J.
1336 Appl. Meteor. Climatol., 50, 399–418, 2011
- 1337 Kneifel, S., von Lerber, A., Tiira, J., Moisseev, D., Kollias, P., and Leinonen, J., Observed relations
1338 between snowfall microphysics and triple-frequency radar measurements. J. Geophys.
1339 Res. Atmos., 120, 6034– 6055, doi: 10.1002/2015JD023156, 2015

- 1340 Kochendorfer, J., Nitu, R., Wolff, M., Mekis, E., Rasmussen, R., Baker, B., and Jachcik, A, Testing
1341 and development of transfer functions for weighing precipitation gauges in WMO-SPICE,
1342 Hydrology and Earth System Sciences, 2, 1437-1452, [https://doi.org/10.5194/hess-22-](https://doi.org/10.5194/hess-22-1437-2018)
1343 1437-2018, 2018
- 1344 Korolev, A. V., E. F. Emery, J. W. Strapp, S. G. Cober, G. A. Isaac, M. Wasey, and D. Marcotte, Small
1345 ice particles in tropospheric clouds: Fact or artifact? Airborne Icing Instrumentation
1346 Evaluation Experiment, Bull. Amer. Meteor. Soc., 92, 967–973,
1347 <https://doi.org/10.1175/2010BAMS3141.1>, 2011
- 1348 Kulie, M. S., and R. Bennartz, Utilizing Spaceborne Radars to Retrieve Dry Snowfall, J. Appl.
1349 Meteor. Climatol., 48, 2564–2580, <https://doi.org/10.1175/2009JAMC2193.1>, 2009
- 1350 Kulie, M. S., Milani, L., Wood, N. B., Tushaus, S. A., Bennartz, R., and L’Ecuyer, T. S., A Shallow
1351 Cumuliform Snowfall Census Using Spaceborne Radar, Journal of Hydrometeorology, 4,
1352 1261-1279, <https://doi.org/10.1175/JHM-D-15-0123.1>, 2016
- 1353 Lawson, R. P., O’Connor, D., Zmarzly, P., Weaver, K., Baker, B., Mo, Q., and Jonsson, H., The 2D-S
1354 (Stereo) Probe: Design and Preliminary Tests of a New Airborne, High-Speed, High-
1355 Resolution Particle Imaging Probe, J. Atmos. Ocean. Tech., 23, 1462–1477,
1356 <https://doi.org/10.1175/JTECH1927.1>, 2006
- 1357 [Liebe, H.J., Manabe, T., and Hufford, G.A., Millimeter–wave attenuation and delay rates due](#)
1358 [fog/cloud conditions, IEEE Trans. Antenn. Propag., 37, 1617–1623, 1989](#)
- 1359 Locatelli, J.D. and Hobbs, P.V., Fall speed and masses of solid precipitation particles, J. Geophys.
1360 Res., 79, 2185–2197, <https://doi.org/10.1029/JC079i015p02185>, 1974
- 1361 Macklin, W.C., The density and structure of ice formed by accretion, Q.J.R.Meteorol.Soc., 88: 30-
1362 50. doi:10.1002/qj.49708837504, <https://doi.org/10.1002/qj.49708837504>, 1962
- 1363 Marlow, S.A, J.M. Frank, M. Burkhart, B. Borkhuu, S.E. Fuller, and J.R. Snider, Snowfall
1364 measurements in mountainous terrain, in revision for the Journal of Applied Meteorology
1365 and Climatology, http://www-das.uwyo.edu/~jsnider/JAMC-D-22-0093_6.pdf, 2023~~2~~
- 1366 Martinaitis, S.M., S.B. Cocks, Y. Qi, B.T. Kaney, J. Zhang, and K. Howard, Understanding winter
1367 precipitation impacts on automated gauge observations within a real-rime system, J.
1368 Hydrometeor., 16, 2345-2363, <https://doi.org/10.1175/JHM-D-15-0020.1>, 2015
- 1369 Mason, S. L., Chiu, C. J., Hogan, R. J., Moisseev, D., and Kneifel, S., Retrievals of riming and snow
1370 density from vertically pointing Doppler radars, Journal of Geophysical Research:
1371 Atmospheres, 123, 13,807– 13,834, <https://doi.org/10.1029/2018JD028603>, 2018
- 1372 Matrosov, S.Y., Modeling Backscatter Properties of Snowfall at Millimeter Wavelengths, J. Atmos.
1373 Sci., 64, 1727-1736, <https://doi.org/10.1175/JAS3904.1>, 2007
- 1374 Moisseev, D., von Lerber, A., and Tiira, J., Quantifying the effect of riming on snowfall using
1375 ground-based observations, J. Geophys. Res. Atmos., 122, 4019–4037,
1376 doi:10.1002/2016JD026272, 2017

- 1377 Panofsky, H.A. and Dutton, J.A., Atmospheric Turbulence, Wiley-Interscience, New York, 397 pp.,
1378 1984
- 1379 Pokharel, B. and G. Vali, Evaluation of Collocated Measurements of Radar Reflectivity and Particle
1380 Sizes in Ice Clouds, J. Appl. Meteor. Climatol., 50, 2104–2119,
1381 <https://doi.org/10.1175/JAMC-D-10-05010.1>, 2011
- 1382 Rasmussen, R.M., J. Hallett, R. Purcell, S.D. Landolt, and J. Cole, The Hotplate precipitation gauge,
1383 J. Atmos. Oceanic Technol., 28, 148-164, <https://doi.org/10.1175/2010JTECHA1375.1>,
1384 2011
- 1385 R.M. Young Company, Model 05103 Wind Monitor, 2001
- 1386 Serreze, M. C., M. P Clark, and R. L. Armstrong, D. A. MacGinnis, and R. S. Pulwarty, Characteristics
1387 of the western United States snowpack from snowpack telemetry (SNOTEL) data, Water
1388 Resources Research, 35, 2145-2160, <https://doi.org/10.1029/1999WR900090>, 1999
- 1389 Skofronick-Jackson, G., and Coauthors, The Global Precipitation Measurement (GPM)
1390 Mission for science and society, Bull. Amer. Meteor. Soc., 98, 1679–1695,
1391 <https://doi.org/10.1175/BAMS-D-15-00306.1>, 2017
1392
- 1393 Smith, P.L., Equivalent radar reflectivity factors for snow and ice particles, J. Climatol. Appl.
1394 Meteor., 23, 1258–1260, [https://doi.org/10.1175/1520-
1395 0450\(1984\)023<1258:ERRFFS>2.0.CO;2](https://doi.org/10.1175/1520-0450(1984)023<1258:ERRFFS>2.0.CO;2), 1984
- 1396 ~~Surussavadee, C. and D.H. Staelin, Comparison of AMSU millimeter-wave satellite observations,
1397 MM5/TBSCAT predicted radiances, and electromagnetic models for hydrometeors, IEEE
1398 Trans. Geosci. Remote Sens., 44, 2667–2678, 10.1109/TGRS.2006.873275, 2006~~
- 1399 Snider, J.R., Supplemental dataset for Marlow et al. (2023), <https://doi.org/10.15786/20247870>,
1400 2023
- 1401 Surussavadee, C., and D. H. Staelin, Millimeter-Wave Precipitation Retrievals and Observed-
1402 versus-Simulated Radiance Distributions: Sensitivity to Assumptions. J. Atmos. Sci., 64,
1403 3808–3826, <https://doi.org/10.1175/2006JAS2045.1>, 2007
- 1404 Tessendorf, S. A., and Coauthors, A transformational approach to winter orographic weather
1405 modification research: The SNOWIE Project, Bulletin of the American Meteorological
1406 Society, 100, 71–92, <https://doi.org/10.1175/BAMS-D-17-0152.1>, 2019
- 1407 Ulaby, F.T., Moore, R.K., and Fung, K., Microwave Remote Sensing: Active and Passive, vol 2,
1408 Addison–Wesley, Advanced Book Program, Reading, MA, p. 456., 1981
- 1409 Vaisala, User’s Guide, Vaisala Weather Transmitter, WXT520, 2012
- 1410 Vali, G. and Haimov, S., Observed extinction by clouds at 95 GHz, IEEE Trans. Geosci. Remote, 39,
1411 190–193, 2001
- 1412

- 1413 Wang, P.K., and W. Ji, Collision Efficiencies of Ice Crystals at Low–Intermediate Reynolds Numbers
1414 Colliding with Supercooled Cloud Droplets: A Numerical Study, *Journal of the Atmospheric*
1415 *Sciences*, 57, 1001-1009, [https://doi.org/10.1175/1520-](https://doi.org/10.1175/1520-0469(2000)057<1001:CEOICA>2.0.CO;2)
1416 [0469\(2000\)057<1001:CEOICA>2.0.CO;2](https://doi.org/10.1175/1520-0469(2000)057<1001:CEOICA>2.0.CO;2), 2000
- 1417 Wilson, J., and E. Brandes, Radar measurement of rainfall—A summary, *Bull. Amer. Meteor. Soc.*,
1418 60, 1048–1058, [https://doi.org/10.1175/1520-0477\(1979\)060<1048:RMORS>2.0.CO;2](https://doi.org/10.1175/1520-0477(1979)060<1048:RMORS>2.0.CO;2),
1419 1979
- 1420 Wolfe, J.P., and J.R. Snider, A relationship between reflectivity and snow rate for a high-altitude
1421 S-band radar, *J. Appl. Meteor. Climatol.*, 51, 1111–1128, [https://doi.org/10.1175/JAMC-](https://doi.org/10.1175/JAMC-D-11-0112.1)
1422 [D-11-0112.1](https://doi.org/10.1175/JAMC-D-11-0112.1), 2012
- 1423 Zaremba, T.J., and Coauthors, Vertical motions in orographic cloud systems over the Payette
1424 River Basin. Part 1: Recovery of vertical motions and their uncertainty from airborne
1425 Doppler radial Velocity Measurements, in press at the *Journal of Applied Meteorology*
1426 *and Climatology*, <https://doi.org/10.1175/JAMC-D-21-0228.1>, 2022
- 1427 Zelasko, N., Wettlaufer, A., Borkhuu, B., Burkhart, M., Campbell, L. S., Steenburgh, W. J., and
1428 Snider, J.R., Hotplate precipitation gauge calibrations and field measurements, *Atmos.*
1429 *Meas. Tech.*, 11, 441-458, <https://doi.org/10.5194/amt-11-441-2018>, 2018
- 1430 Zikmunda, J. and Vali, G., Fall patterns and fall velocities of rimed ice crystals, *J. Atmos. Sci.*, 29,
1431 1334–1347, [https://doi.org/10.1175/1520-0469\(1972\)029<1334:FPAFVO>2.0.CO;2](https://doi.org/10.1175/1520-0469(1972)029<1334:FPAFVO>2.0.CO;2),
1432 1972

Table 3 – Attenuating component concentration, one-way pathlength, and summed two-way attenuation

Date	Conc. Vapor, kg m^{-3}	Conc. Cloud Water, kg m^{-3}	Conc. Snow Particles, kg m^{-3}	Pathlength Vapor, km	Pathlength Cloud Water, km	Pathlength Snow Particles, km	Overall Two-way Attenuation, dB
15 December 2016	2.7×10^{-3}	0.01×10^{-3}	0.10×10^{-3}	1.54	1.09	1.54	0.82 ^a
3 January 2017	1.8×10^{-3}	0.08×10^{-3}	0.05×10^{-3}	1.19	0.59	1.19	0.82 ^b

^a One-way attenuation coefficients are 0.14 dB/km for vapor (Ulaby et al. 1981), 0.052 dB/km for cloud water (Liebe et al. 1989; Vali and Haimov 2001), and 0.085 dB/km for snow particles (Nemarich et. al 1988).

^b One-way attenuation coefficients are 0.073 dB/km for vapor (Ulaby et al. 1981), 0.45 dB/km for cloud water (Liebe et al. 1989; Vali and Haimov 2001), and 0.045 dB/km for snow particles (Nemarich et. al 1988).

